



HAL
open science

Spatiotemporal patterns of terrestrial gross primary production: A review

Alessandro Anav, Pierre Friedlingstein, Chris Beer, Philippe Ciais, Anna Harper, Chris R Jones, Guillermo Murray-Tortarolo, Dario Papale, Nicholas Parazoo, Philippe Peylin, et al.

► To cite this version:

Alessandro Anav, Pierre Friedlingstein, Chris Beer, Philippe Ciais, Anna Harper, et al.. Spatiotemporal patterns of terrestrial gross primary production: A review. *Reviews of Geophysics*, 2015, 53 (3), pp.785 - 818. 10.1002/2015RG000483 . hal-01805714

HAL Id: hal-01805714

<https://hal.science/hal-01805714>

Submitted on 28 Oct 2020

HAL is a multi-disciplinary open access archive for the deposit and dissemination of scientific research documents, whether they are published or not. The documents may come from teaching and research institutions in France or abroad, or from public or private research centers.

L'archive ouverte pluridisciplinaire **HAL**, est destinée au dépôt et à la diffusion de documents scientifiques de niveau recherche, publiés ou non, émanant des établissements d'enseignement et de recherche français ou étrangers, des laboratoires publics ou privés.



REVIEW ARTICLE

10.1002/2015RG000483

Key Points:

- At global scale, direct measurements of GPP do not exist
- Large uncertainties exist on terrestrial global GPP benchmarking
- Models show large variability in mean global GPP estimates

Correspondence to:

A. Anav,
A.Anav@exeter.ac.uk

Citation:

Anav, A., et al. (2015), Spatiotemporal patterns of terrestrial gross primary production: A review, *Rev. Geophys.*, 53, 785–818, doi:10.1002/2015RG000483.

Received 3 MAR 2015

Accepted 23 JUN 2015

Accepted article online 27 JUN 2015

Published online 18 AUG 2015

Spatiotemporal patterns of terrestrial gross primary production: A review

Alessandro Anav¹, Pierre Friedlingstein¹, Christian Beer², Philippe Ciais³, Anna Harper¹, Chris Jones⁴, Guillermo Murray-Tortarolo¹, Dario Papale^{5,6}, Nicholas C. Parazoo⁷, Philippe Peylin³, Shilong Piao⁸, Stephen Sitch⁹, Nicolas Viovy³, Andy Wiltshire⁴, and Maosheng Zhao¹⁰

¹College of Engineering, Mathematics and Physical Sciences, University of Exeter, Exeter, UK, ²Department of Applied Environmental Science (ITM) and Bolin Centre for Climate Research, Stockholm University, Stockholm, Sweden,

³Laboratoire des Sciences du Climat et de l'Environnement, Gif sur Yvette, France, ⁴Met Office Hadley Centre, Exeter, UK,

⁵Department for Innovation in Biological, Agro-Food and Forest Systems, University of Tuscia, Viterbo, Italy, ⁶CzechGlobe – Global Change Research Centre AS CR, Brno, Czech Republic, ⁷Jet Propulsion Laboratory, California Institute of Technology, Pasadena, California, USA, ⁸Key Laboratory of Alpine Ecology and Biodiversity, Institute of Tibetan Plateau Research, Chinese Academy of Sciences, Beijing, China, ⁹College of Life and Environmental Sciences, University of Exeter, Exeter, UK,

¹⁰Department of Geographical Sciences, University of Maryland, College Park, Maryland, USA

Abstract Great advances have been made in the last decade in quantifying and understanding the spatiotemporal patterns of terrestrial gross primary production (GPP) with ground, atmospheric, and space observations. However, although global GPP estimates exist, each data set relies upon assumptions and none of the available data are based only on measurements. Consequently, there is no consensus on the global total GPP and large uncertainties exist in its benchmarking. The objective of this review is to assess how the different available data sets predict the spatiotemporal patterns of GPP, identify the differences among data sets, and highlight the main advantages/disadvantages of each data set. We compare GPP estimates for the historical period (1990–2009) from two observation-based data sets (Model Tree Ensemble and Moderate Resolution Imaging Spectroradiometer) to coupled carbon-climate models and terrestrial carbon cycle models from the Fifth Climate Model Intercomparison Project and TRENDY projects and to a new hybrid data set (CARBONES). Results show a large range in the mean global GPP estimates. The different data sets broadly agree on GPP seasonal cycle in terms of phasing, while there is still discrepancy on the amplitude. For interannual variability (IAV) and trends, there is a clear separation between the observation-based data that show little IAV and trend, while the process-based models have large GPP variability and significant trends. These results suggest that there is an urgent need to improve observation-based data sets and develop carbon cycle modeling with processes that are currently treated either very simplistically to correctly estimate present GPP and better quantify the future uptake of carbon dioxide by the world's vegetation.

1. Introduction

At leaf level, terrestrial plants fix atmospheric carbon dioxide (CO₂) as organic compounds by net photosynthesis; at ecosystem scale, the gross uptake of CO₂ is known as gross primary production (GPP) (i.e., the sum of the net photosynthesis by all leaves measured at the ecosystem scale) [Chapin et al., 2002; Beer et al., 2010]. Both leaf photosynthesis and GPP vary diurnally and seasonally in response to changes in climate (light, precipitation, temperature, and humidity) and nutrient availability, while the spatial distribution is determined primarily by climatic conditions.

Terrestrial GPP is the major driver of land carbon sequestration and it plays a pivotal role in the global carbon balance, providing the capacity of terrestrial ecosystems to partly offset anthropogenic CO₂ emissions [Janssens et al., 2003; Cox and Jones, 2008; Battin et al., 2009].

Given its central role in the global carbon budget and the increasing need to understand the role of the terrestrial biosphere in global carbon cycle, it is critical to develop a clear understanding of GPP spatiotemporal patterns [Canadell et al., 2000]. Therefore, the quantification of GPP is becoming a major topic in global climate change studies.

However, direct measurements of GPP do not exist because no observation techniques are available to quantify this process at the right spatial scale [Ma et al., 2015]. Using photosynthesis measurements at leaf

©2015. The Authors.

This is an open access article under the terms of the Creative Commons Attribution-NonCommercial-NoDerivs License, which permits use and distribution in any medium, provided the original work is properly cited, the use is non-commercial and no modifications or adaptations are made.

level is not that straightforward because of difficulties in controlling environmental conditions of gas exchange chambers or physical placement of a cuvette on a leaf (or a chamber over a plant) that may produce biases and artifacts [Baldocchi, 2003]. Nevertheless, one can reduce the experimental artifacts introduced by cuvettes by controlling the temperature, light, CO₂, and humidity. However, even when direct photosynthesis measurements can be made, they usually represent small samples in space and time [Ryan, 1991; Long and Bernacchi, 2003].

GPP can be only inferred from direct measurements of net carbon exchange between terrestrial ecosystems and the atmosphere [Reichstein et al., 2005; Lasslop et al., 2010; Reichstein et al., 2012] at ecosystem scale, while at a larger scale even more assumptions have to be taken into account [Jung et al., 2009; Beer et al., 2010; Jung et al., 2011].

Worldwide more than 600 measuring flux tower stations exist (<http://fluxnet.ornl.gov/>) for the measurement of CO₂ exchange between ecosystems and the atmosphere through the eddy covariance technique [Baldocchi et al., 2001; Friend et al., 2007; Aubinet et al., 2012]. This method allows quantification of the continuous net ecosystem exchange (NEE) of CO₂, namely, the balance between the carbon released by ecosystems through the respiration and the carbon uptake by GPP. For each flux tower station, several algorithms allow separation of ecosystem respiration (R_{eco}) and GPP from NEE [Reichstein et al., 2005; Reichstein et al., 2012] through relatively simple models parameterized with the NEE measurements.

However, the component fluxes of NEE (i.e., GPP and R_{eco}) cannot be measured directly at a regional or global scale. Thus, to retrieve GPP estimates at larger scales, available local flux tower observations have been scaled up to the globe using data-driven (or statistical) models [Jung et al., 2009; Beer et al., 2010; Jung et al., 2011].

The data-driven modeling based on eddy covariance technique comprises two steps: (1) the parameterization of GPP in relation to explanatory variables at sites and (2) the application of the model using gridded information about these explanatory variables. In the first step, the GPP estimated by partitioning continuous NEE measurements is used to establish the relation between local drivers and flux, while with the second step the spatial and temporal variability of GPP is computed using gridded remote sensing and climatic data [Jung et al., 2009].

There exist several data-driven methods on scaling eddy covariance-based information to the globe including pure statistical methods (such as neural networks or model trees) or semiempirical regression models, based on inherent water-use efficiency [Beer et al., 2009] or light use efficiency [Monteith, 1972, 1977]. However, all these approaches have a low capacity in extrapolating to completely different environmental conditions, and it depends on the availability of sufficient data [Beer et al., 2010]. In addition, these models are not able to extrapolate in time, i.e., to predict future fluxes.

Another data-driven approach to quantify variations in GPP at global scales is based on satellite measurements of optical parameters that are directly related to vegetation activity [Myneni et al., 2002; Damm et al., 2010]. Different remote sensing-based GPP models have been proposed; in general, these GPP models can be classified into two categories. One major type of remotely sensed GPP includes models that employ the maximum light use efficiency (LUE) [Monteith's, 1972, 1977; Goetz and Prince, 1999; Turner et al., 2005; Hilker et al., 2008]. The other major model type uses remotely sensed leaf area index (LAI) to scale-up Farquhar photosynthesis model [Farquhar et al., 1980] from leaf level to canopy and then to regional or global level [Chen et al., 2012; Ryu et al., 2011]. The former LUE-type method is more straightforward and simple but often yields insufficient results, because it measures only the absorbed photosynthetically active radiation (APAR) while assuming LUE to be constant or it is modeled from ancillary meteorological variables [Goetz and Prince, 1999].

Alternatively, considerable efforts have been made to develop process-based carbon cycle models to understand terrestrial carbon cycle mechanisms at different spatial scales [Moorcroft, 2006; Prentice et al., 2014, and references therein]. Process-based terrestrial carbon models, simulating the major processes of the carbon cycle, have been used to study the role of the terrestrial biosphere in the global carbon cycle and to assess possible future changes and risks in biogeochemical cycles associated with a changing climate [Cramer et al., 1999; Kicklighter et al., 1999; Cramer et al., 2001; McGuire et al., 2001; Dargaville et al., 2002; Sitch et al., 2003; Morales et al., 2005; Zaehle et al., 2007; Sitch et al., 2008; Le Quéré et al., 2009; Piao et al., 2009].

A broad range of models now exists, ranging in complexity from simple regressions based on climatic variables [e.g., *Agreen et al.*, 1991; *McGuire et al.*, 1993] to complex models that simulate biophysical and ecophysiological processes [e.g., *Sitch et al.*, 2003; *Krinner et al.*, 2005]. Each approach is based on simplifying assumptions about how ecosystems are structured and how vegetation responds to changes in the environment. However, since ecosystems are highly complex, it is impossible to include all component processes and their interactions into a numerical model, and thus, simplifications must be made.

Different sets of equations, parameter values, and forcing variables thus lead to different estimates of GPP or more generally to different model behaviors. The differences in models' results due to only differences in the equations are often referred to as structural uncertainty [*Wang et al.*, 2011; *Zhao et al.*, 2012].

Consequently, terrestrial carbon cycle models used to assess the effect of past or future climate scenarios on ecosystems need to be systematically evaluated to ensure that they are able to correctly simulate the seasonal cycles, interannual variability, and trends of carbon fluxes [*Anav et al.*, 2013]. It is also necessary to identify the sources of variation between models and between models and observations that could help modelers identify shortcomings and improve their tools [*Morales et al.*, 2005].

One prerequisite for the analysis of spatiotemporal biosphere-atmosphere fluxes is the comparison of GPP simulated by different models [*Vetter et al.*, 2008; *Jung et al.*, 2008]. In fact, since GPP is directly sensitive to variations in carbon dioxide concentration and climate, conducting comparative investigations of terrestrial models reveals the effects of different model structures [*Richardson et al.*, 2006], parameter values [*Braswell et al.*, 2005; *Zaehle et al.*, 2005], input climate forcing [*Zhao et al.*, 2006; *Lin et al.*, 2011; *Zhao et al.*, 2012], and initial states of biomass and soil carbon pools [*Carvalho et al.*, 2008]. In addition, comparing models with data is useful for understanding the behavior of both models and data in a joint perspective [*Betts*, 2004; *Jaeger et al.*, 2009; *Mahecha et al.*, 2010].

One major source of uncertainty in carbon cycle modeling is the meteorological forcing field used to run these models. The choice of the meteorological input data set alone can result in a typical 20% difference of simulated GPP [*Zhao et al.*, 2006; *Jung et al.*, 2007], and it can strongly influence the spatial patterns of modeled GPP [*Jung et al.*, 2007; *Poulter et al.*, 2011].

Recently, a consortium of terrestrial carbon cycle modeling groups agreed to investigate the spatial trends in land-atmosphere carbon flux by performing a set of simulations in which all the models were forced by the same observed climate over the historical period 1901–2010 (TRENDY project [*Sitch et al.*, 2015]). The availability of different terrestrial carbon models forced by the same input data removes the uncertainty due to the different meteorological forcing fields. However, even when using a particular forcing there can be systematic errors that will be propagated to the output of carbon models.

In contrast, Earth System Models (ESMs) have been developed mainly during the last decade [*Collins et al.*, 2011; *Gent et al.*, 2011; *Watanabe et al.*, 2011; *Dunne et al.*, 2012; *Bentsen et al.*, 2013; *Dufresne et al.*, 2013; *Ji et al.*, 2014]; within an ESM, a given process-based terrestrial carbon model is fully coupled to a climate model. In other words, like offline simulations (i.e., models using prescribed forcings), the simulated climate impacts GPP, but unlike offline models, the state of the vegetation (i.e., phenology, surface energy fluxes, and greenhouse gas sources and sinks) also modifies the climate leading to a high temporal consistency between the atmosphere and the land surface. ESMs further incorporate additional components such as atmospheric chemistry, aerosols, and the oceanic carbon cycle [*Taylor et al.*, 2012].

The ESMs are forced by a variety of externally imposed changes such as increasing greenhouse gas (concentration-driven simulations [*Taylor et al.*, 2012]) and sulfate aerosol concentrations, changes in solar radiation, and forcing by volcanic eruptions. These prescribed forcings allow the models to compute their own climate with their interannual variability [*Lin*, 2007].

It should be noted that some of these ESMs simulate the terrestrial carbon cycle with the same carbon cycle models used in TRENDY. Thus, the existence of different land carbon models that use the same prescribed climate (i.e., TRENDY) represents a unique opportunity to separate and compare the effects on GPP of differences in climate simulated by ESMs against the effect of structural differences in the carbon models. In other words, comparing different terrestrial carbon cycle models forced by the same climatic forcing allows the identification of structural model uncertainties (systematic and random), while comparing the carbon models when they are coupled within ESMs allows the identification of climate forcing-related uncertainties on GPP.

A hybrid approach for quantifying CO₂ surface fluxes has been proposed, merging carbon fluxes measurements with process-based models [Rayner *et al.*, 2005]. This method is based on data assimilation, namely, the process of finding the model representation that is most consistent with observations. In other words, the data assimilation is generally used to find an optimal combination of models' parameter values that minimize a function which describes the misfits between observation and model results.

Given the relevant role of GPP in the global carbon balance as well as the limitations of existing data sets, there has been much effort to provide empirical-based constraints [Frankenberg *et al.*, 2011]. Here we compare GPP estimates for the period 1990–2009 from different observation-based data sets (model tree ensemble (MTE) and Moderate Resolution Imaging Spectroradiometer (MODIS)), different coupled carbon-climate models and terrestrial carbon models from the Fifth Climate Model Intercomparison Project (CMIP5) and TRENDY projects, and a new hybrid data set (CARBONES) to identify the agreement between them as well as the strength and weakness of each product. In fact, none of the available data sets is based only on measurements, but assumptions must be made to retrieve the final value one way or another. In other words, all the available estimates have a modeling component behind; thus, each data set has some advantages/limitations.

Despite the existence of many different models from TRENDY simulations, only few of them are actually used online within an ESMs; thus, here we present results for the only TRENDY models that have also been used as land component within an ESM. This analysis is supported and reinforced by recent results of Dalmonech *et al.* [2015] who demonstrated that comparing a coupled and an uncoupled configuration of the same model helps to isolate climate model from land model biases.

2. Available Global GPP Products

2.1. Observation-Based GPP

We use two different observation-based data sets: the first one is a data-driven model based on eddy covariance data, while the second data set is a data-driven model based on satellite measurements.

2.1.1. Data-Driven GPP Trained by Eddy Covariance Measurements

The first data set (MTE-GPP) is a statistical model of GPP based upon flux tower local observations, global satellite retrievals of fraction of absorbed photosynthetically active radiation (fAPAR), and global climate fields. This model uses a model tree ensemble (hereafter MTE) which is a machine learning system where the target variable (i.e., GPP) is predicted by a set of multiple linear regressions from explanatory variable. This model has been recently applied to the upscaling of water and carbon fluxes [Jung *et al.*, 2009, 2011].

GPP estimates were derived at site level by eddy covariance measurements from 178 of the stations belonging to the LaThuile Collection [Jung *et al.*, 2009; Beer *et al.*, 2010; Jung *et al.*, 2011].

The eddy covariance measurements at the basis of this product were collected and harmonized in the LaThuile FLUX NETwork (FLUXNET) Synthesis database (www.fluxdata.org). The data were processed with standard methodologies, including quality filtering and partitioning of NEE in the two components (GPP and ecosystem respiration). The GPP estimates were aggregated at different time resolutions and then used to parameterize the data-driven models together with the drivers either measured at the site (climatic data) or extracted at the tower location (remote sensing data).

Specifically, two steps are required to produce global GPP estimates from local site measurements: in the first step the model tree ensemble is trained against eddy covariance GPP estimates at site level using satellite observations of fAPAR and meteorological data as explanatory variables. In the second step, global explanatory variables are used in combination to the trained MTE-GPP to estimate global GPP patterns [Jung *et al.*, 2009, 2011].

This data set provides GPP estimates at a spatial resolution of 0.5° × 0.5° and with monthly time step for the temporal period 1982–2011 [Jung *et al.*, 2011]. Although the MTE data set starts in 1982, it is important to note that since FLUXNET site measurements only began in the mid-1990s with just few tens of sites mainly in Europe and USA, the extrapolation of GPP back to 1990s is based on the sensitivity of GPP to climate. In addition, most of the eddy covariance stations available are in Europe and North America, so that the MTE-GPP is poorly constrained by observations in Tropical, Boreal, and Siberian regions. This latter point suggests that there is large uncertainty in the regions that are not covered by measurement stations (e.g., Africa, Siberia, South America, and Tropical Asia).

Another source of uncertainty in the MTE-GPP might be the lack of CO₂ fertilization: in fact, while atmospheric CO₂ rose from about 340 until 390 ppm during our study period, the MTE assumes an average CO₂ level not increasing with time.

The estimated uncertainty of global mean annual GPP ($\sim 6 \text{ Pg C yr}^{-1}$ [Jung *et al.*, 2011]) was quantified based on the standard deviation over the ensemble of 25 different trees. However, this value does not consider other sources of uncertainty such as the uncertainty from the eddy covariance fluxes measurements and their partitioning as well as the uncertainty of global satellite observations of fAPAR and meteorological data used as predictor variables.

2.1.2. Data-Driven GPP Trained by Satellite Measurements

The second data set we used is the improved Moderate Resolution Imaging Spectroradiometer (MODIS) GPP [Zhao *et al.*, 2006; Zhao and Running, 2010]. MODIS, which provides a quantitative and dynamic measurement of spatial and temporal productivity by vegetation, is a continuous satellite-driven data set monitoring global vegetation at 1 km resolution. It provides 8 day, monthly, and annual data over the period 2000–2012 (<http://www.nts.gov/project/mod17>).

The MODIS GPP algorithm is described in Running *et al.* [2004]. A simple light use efficiency model (MOD17) is at the core of the GPP component of the algorithm, and it requires daily inputs of incoming photosynthetically active radiation and climatic variables. MODIS GPP data are driven by National Centers for Environmental Prediction–Department of Energy (NCEP-DOE) II meteorological reanalysis data set [Zhao and Running, 2010]. Additional MOD17 inputs include fAPAR and LAI, which are both standard MODIS products.

Unlike the MTE algorithm that allows the uncertainty of the data set to be estimated, for the MODIS data it is challenging to quantify the uncertainties in GPP estimates, because first, there are no quantified uncertainties in most of the input data, such as weather data from NCEP-DOE II, and second, our knowledge on the uncertainties in the biome property parameters are still poor [Zhao and Running, 2011]. Uncertainties in the inputs from MODIS land cover, fAPAR/LAI, daily meteorological data, GPP algorithm, and its parameters thus can introduce uncertainties in the estimated MODIS GPP [Zhao *et al.*, 2005].

In addition, cautions should be taken for comparing satellite estimates with model-simulated GPP. In fact, remotely sensed fAPAR generally provides key realistic spatiotemporal changes of vegetation leaf area and cover because disturbances, recovery, and human management can be directly detected though resolution dependent. Thus, resulting GPP can largely reflect either the reduction in plant growth caused by deforestation, desertification, and disturbances (fires, wind throw, insects' outbreaks, and storms) or the enhancement in vegetation growth caused by reforestation, fertilizer users, and effects of nitrogen deposition. In contrast, GPP estimated by many process-based models simulates potential LAI when an ecosystem reaches an equilibrium status under the input climate and soil conditions. Human activities tend to reduce vegetation cover (LAI), and many ecosystems cannot reach equilibrium status due to extensive human interferences. Therefore, in principle, if both remotely sensed GPP and process-based models are perfect and input data sets are accurate, modeled GPP is generally higher than remotely sensed GPP.

2.2. Process-Based Models

2.2.1. Land Carbon Models (Offline Models)

We use monthly GPP output from terrestrial carbon models that took part in TRENDY project [Sitch *et al.*, 2015]. Results are from the so-called "S3" TRENDY simulation which uses observed CO₂ concentrations, climate, and land cover change as forcing over the period 1901–2010. The same 6-hourly climate data from the Climate Research Unit (CRU)-NCEP climate forcing [Wei *et al.*, 2014] were used in all models.

Although many different models from TRENDY simulations exist, due to the unavailability of the corresponding online version, we used only three different models.

In the first model, Community Land Model Carbon-Nitrogen version 4 (CLMCN4) [Thornton and Rosenbloom, 2005; Thornton *et al.*, 2007, 2009; Randerson *et al.*, 2009], photosynthesis by plants adopting the C₃ biochemical pathway [Chapin *et al.*, 2002] is based on the model of Farquhar *et al.* [1980] as modified by Collatz *et al.* [1991], while for plants adopting the C₄ biochemical pathway it is based on the model of Collatz *et al.* [1992].

Table 1. Summary of the Land Models Used With the Associated Original Resolution and Main Features Controlling the Terrestrial Carbon Cycle^a

	Offline (TRENDY)			Online (CMIP5)			
	CLM4CN	JULES	ORCHIDEE	CESM1-BGC	HadGEM2-ES	IPSL-CM5A-MR	NorESM1-ME
Spatial resolution (longitude × latitude)	0.5° × 0.5°	1.85° × 1.25°	0.5° × 0.5°	0.9° × 1.25°	1.875° × 1.25°	2.5° × 1.25°	2.5° × 1.9°
Land area (60°S–90°N)	1.359E+14 m ²	1.333E+14 m ²	1.343E+14 m ²	1.347E+14 m ²	1.335E+14 m ²	1.381E+14 m ²	1.347E+14 m ²
Number of PFTs	16	5	13	15	5	13	15
Dynamic vegetation	N	N	N	N	Y	N	N
N Cycle	Y	N	N	Y	N	N	Y
Land component	Valid only for the online models			CLM4CN	JULES	ORCHIDEE	CLM4CN
Atmospheric forcing	CRU-NCEP			CAM4	HadGEM2	LMDZ	CAM4-Oslo
Photosynthesis for C3 PFTs	<i>Collatz et al.</i> [1991]	<i>Collatz et al.</i> [1991]	<i>Farquhar et al.</i> [1980]	Same as the offline models			
Photosynthesis for C4 PFTs	<i>Collatz et al.</i> [1992]	<i>Collatz et al.</i> [1992]	<i>Collatz et al.</i> [1992]				
Reference	<i>Oleson et al.</i> [2010]	<i>Clark et al.</i> [2011]	<i>Krinner et al.</i> [2005]	<i>Gent et al.</i> [2011]	<i>Collins et al.</i> [2011]	<i>Dufresne et al.</i> [2013]	<i>Bentsen et al.</i> [2013]

^aPFT, plant functional type; Y, yes; N, no.

The second model, Joint UK Land Environment Simulator (JULES) [Best et al., 2011; Clark et al., 2011], uses the biochemistry of C₃ and C₄ photosynthesis from Collatz et al. [1991, 1992], as described by Sellers et al. [1992] and Cox et al. [1999], to determine potential leaf-level photosynthesis [Clark et al., 2011].

In the third model, ORganizing Carbon and Hydrology in Dynamic EcosystEms (ORCHIDEE) [Krinner et al., 2005], the C₃ and C₄ photosynthesis is calculated following Farquhar et al. [1980] and Collatz et al. [1992], respectively.

The models differ in their resolution, their parameterization, and the way they simulate several processes. Table 1 lists the models used in this study, while a detailed discussion on the way they calculate GPP is given in Appendix A.

2.2.2. Earth System Models (Online Models)

We examine GPP as simulated by ESMs from the Fifth Climate Model Intercomparison Project (CMIP5). As the TRENDY project, also ESMs from CMIP5 use common simulation and output protocols, enabling direct comparisons between models.

Here we use results from “historical” runs [Taylor et al., 2012], in which the ESMs were forced by increasing greenhouse gas and sulfate aerosol concentrations, changes in solar radiation, forcing by volcanic aerosols, and time-evolving land use changes. Simulations for the historical period extend from 1850 to 2005. Since our reference period for the analysis is 1990–2009, we used results from RCP 2.6 to fill the period 2006–2009. In fact, this RCP has the CO₂ concentration closer to the observed levels during this period. It should also be noted that the difference between all the existing RCPs is not large during the first years of simulation.

Four CMIP5 ESMs are selected based on the availability of the same land component of the TRENDY models: CLM4CN is the land model component of the Community Earth System Model (CESM1-BGC [Gent et al., 2011]) and Norwegian Earth System Model (NorESM1-ME [Bentsen et al., 2013]), ORCHIDEE is the land component of the IPSL-CM5A-MR Earth system model [Dufresne et al., 2013], while JULES is used in the Hadley Centre climate model HadGEM2-ES [Johns et al., 2006; Collins et al., 2011].

2.3. Hybrid GPP

A third data set (CARBONES) that couples a process-based carbon cycle models (ORCHIDEE) with global carbon cycle data assimilation system has been recently designed to estimate the net CO₂ fluxes over land and ocean from regional to global scales for the past 20 years (1990–2009). It uses data from both in situ measuring stations (FLUXNET, global CO₂ networks, biomass, and soil inventories) as well as satellite data of land and oceanic properties, including the atmospheric composition [Kuppel et al., 2013].

CARBONES is based on three different models that describe the global carbon cycle: LMDz [Hourdin *et al.*, 2006] is used to describe the concentration and transport of CO₂ into the atmosphere, ORCHIDEE [Krinner *et al.*, 2005] simulates the sink and sources of carbon over the land, and a simplified statistical model simulates the ocean carbon cycle [Kuppel *et al.*, 2013]. All these models are optimized with a data assimilation system by using satellite and in situ observations [Kuppel *et al.*, 2013].

As with MTE-GPP, CARBONES uses flux tower measurements to constrain GPP (about 60 sites, mostly over Northern Europe and America); thus, in the regions where no GPP data from flux tower are available, the uncertainties are higher. In addition, it should be noted that in these regions, CARBONES is not independent from ORCHIDEE; namely, it is ORCHIDEE in areas that are not informed by data; thus in the following analysis we expect a close similarity between ORCHIDEE and CARBONES GPPs.

3. Spatiotemporal Pattern of GPP

Processes within the models are simulated on a per area basis. In other words, the carbon stores and fluxes are calculated with units of per square meter. This allows the models to be developed without need to know their eventual spatial resolution and to be evaluated against site level, flux tower data. However, when they are run in gridded mode these fluxes must be scaled by the land area in order to estimate a global total. In addition, for coupled ESMs, this area-scaled global flux is what matters to drive the model's evolution of atmospheric CO₂. Table 1 shows that there is some discrepancy between models in their representation of the global land area up to 3.5% difference. Although these differences are much smaller than the between-model differences in GPP per unit area that will be shown in this section, it still represents a difference of several Pg C yr⁻¹ for the global mean GPP. Similar arguments hold for all other carbon stores and fluxes, so that total land carbon stored in CMIP5 ESMs may differ by as much as 100 PgC due to differences in the models land area. In order to remove this issue in our subsequent analysis, for the results presented here, we regrid all the data sets onto a common 1° × 1° grid.

3.1. Annual Means

Figure 1 shows the spatial distributions of mean annual GPP from the models, the observation-based data sets, and a hybrid product over the period 1990–2009; however, in case of MODIS, due to the lack of data before the year 2000, we show data only over the period 2000–2009.

The global spatial patterns from MTE, MODIS, and CARBONES agree reasonably well, although differences are significant in some areas. Specifically, there is a good agreement in boreal regions, but CARBONES estimates higher GPP than MTE and MODIS over Central Europe, southeastern Asia, and in the whole tropical band.

The largest differences in magnitude are found in the Tropics where CARBONES predicts more than 3500 g C m⁻² yr⁻¹ over the whole Amazonian region, while MTE and MODIS have weaker GPP, typically below 3000 g C m⁻² yr⁻¹. Since neither MODIS nor MTE makes use of any artificial cap, such large differences can be due to discrepancies in the weather data [Zhao *et al.*, 2006] or to the lack of or coarse parameterization of disturbances in CARBONES (as already discussed in section 2.1.2).

This pattern is consistent with the finding by Zhao *et al.* [2006], which showed that the tropical region has the largest uncertainties in GPP. In addition, it should be noted that for both CARBONES and MTE most of the uncertainty is due to the limited number of flux sites available over the tropical region, while MODIS could be affected by cloud cover, although data affected by excessive cloudiness have been filled with data from a cloud-free period [Zhao *et al.*, 2005].

Consistent with the observation-based data and CARBONES, all the models show that the largest GPP fluxes occur in the Tropics followed by monsoonal subtropical regions (e.g., South and East Asia), humid temperate regions in Eastern North America, and Western and Central Europe. Low GPPs are typical of adverse environments, such as high latitudes characterized by a short growing season and low temperatures, or dry areas where the water availability limits the plant production. In addition, the models correctly capture the GPP pattern over the boreal region; namely, boreal forests have a typical longitudinal gradient in Northern Eurasia with GPP decreasing toward the East as a consequence of increasingly continental climate [Beer *et al.*, 2010].

However, it is noteworthy that some clear differences exist: specifically, compared to other data sets CLM4CN and HadGEM2-ES exhibit larger GPP (both in terms of magnitude and extension) over the whole Southern

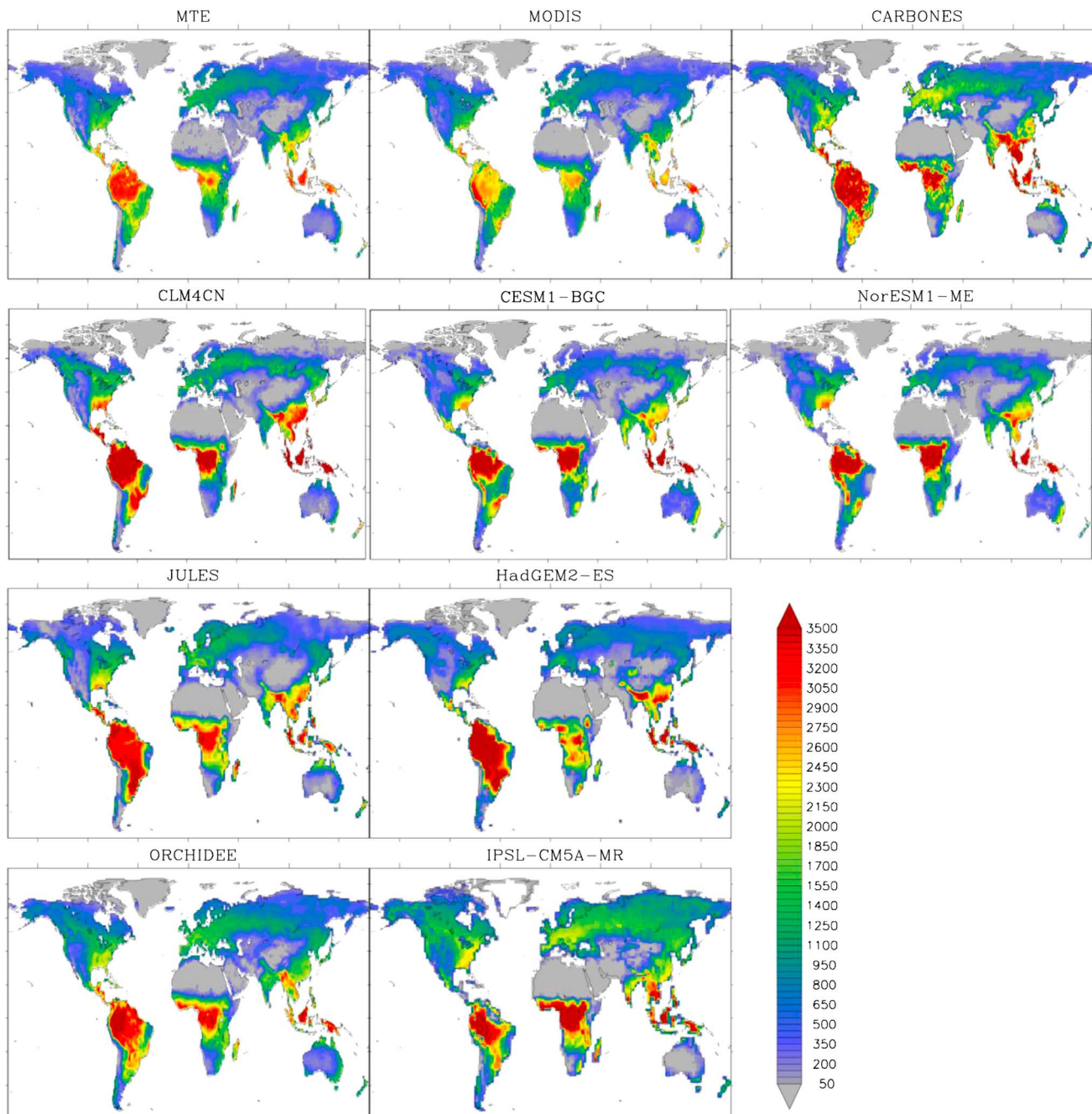


Figure 1. Spatial distribution of mean annual GPP ($\text{g C m}^{-2} \text{yr}^{-1}$) computed over the period 1990–2009 by CMIP5 and TRENDY models, observation-based data (MTE and MODIS), and a hybrid data set (CARBONES).

America, while IPSL-CM5A-MR shows high GPP values over the boreal and arctic regions of Northern Hemisphere. Since ORCHIDEE does not show the same pattern over these regions, the larger GPP found in IPSL-CM5A-MR is likely related to the high positive bias in surface temperature simulated by this Earth system model [Dufresne et al., 2013].

In order to detect the main discrepancy among different data sets, in Figure 2 we shows zonal means of mean annual GPP. The latitudinal gradient of mean annual GPP follows the overall distribution of biomes with GPP increasing from dry and cold biomes (desert and tundra) to warm and moist biomes (temperate and tropical forests).

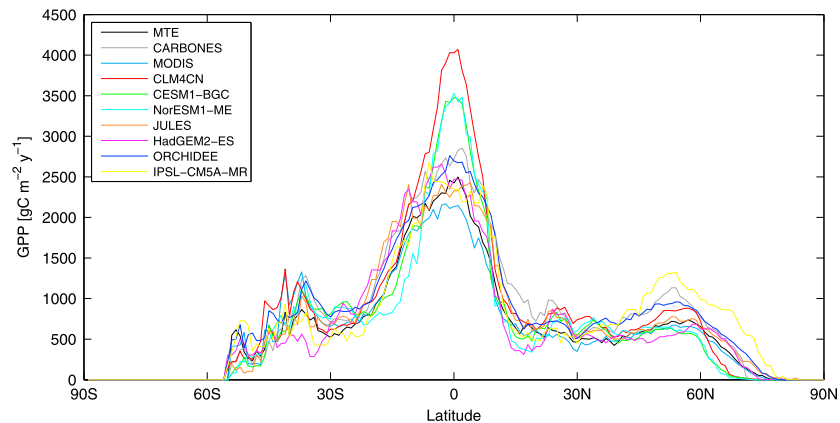


Figure 2. Comparison of the climatological zonal mean computed over the period (1990–2009) for the different models, observation-based data, and a hybrid data set.

In the equatorial zone (10°S–10°N), all the data sets show a peak in GPP, reflecting the abundance of environmental resources available for plant production (water, light, temperature, and nitrogen for models including the N cycle). In the dry tropics (10°S–25°S and 10°N–25°N), all the different data sets exhibit a dip in GPP due to a water shortage. Finally, in the temperate zone of the two hemispheres all the data sets show a secondary peak, due to the availability of water.

However, there is also a considerable variability in the magnitude of annual GPP among all the different estimates, particularly around the main two zonal peaks: mean annual GPP in tropical area (around the equator) was the most variable among models, observation-based data sets, and the hybrid product, with CLM4CN being the most productive model, while MODIS gives the lower estimates. While in the Tropics CLM4CN has been found systematically at the upper bound of TRENDY models [Parazoo *et al.*, 2014], a previous study shows that MODIS GPP is smaller than the GPP estimated at some flux tower stations [Heinsch *et al.*, 2006].

Although there is a good agreement between the observation-based data sets and the hybrid data in the temperate and subtropical areas, over the tropical region these data sets suffer of large uncertainty: specifically looking at the equator, MODIS shows a peak around 2100 gC m⁻² yr⁻¹ while MTE and CARBONES have a peak at 2500 and 2700 gC m⁻² yr⁻¹, respectively.

The relatively low MODIS GPP in the tropics may arise from a low-average annual total GPP set for major tropic biomes, such as evergreen broad leaf forest, woody savannahs, and savannahs, when calibrating the parameters of MODIS GPP or net primary production (NPP); this is partially supported by a recent validation work in Africa [Sjöström *et al.*, 2013] which shows how MODIS underestimates GPP compared to 12 eddy covariance flux towers. Considering MTE and CARBONES, most of the uncertainty is due to the limited number of flux sites available over tropics. In contrast, the models range between MTE and CARBONES, with only CLM-based models falling outside this range.

To further investigate the relationship between climatic controls and productivity, we plotted for each model and data set the mean annual GPP in the climate space of temperature, precipitation, and radiation for each grid cell (Figure 3). As previously discussed, ESMs produce their own climate with the atmospheric model, while offline models are all forced by CRU-NCEP. Similarly, MTE uses CRU for the upscaling of fluxes, while MODIS is driven by DOE II meteorological reanalysis data set. It should also be noted that Zhao and Running [2010] reported small discrepancies between CRU and DOE data.

The overall picture of GPP distribution in the climate space is quite homogeneous among the different data sets, even though some differences exist and a few outlier values were detected. The lowest GPP are found in environments characterized by low temperatures, or with high temperatures but limited by moisture availability (i.e., low precipitation).

These low-productivity ecosystems correspond to high-latitude biomes, such as tundra with negative mean annual temperatures ranging from 0 to –10°C, or desert areas, where the temperature is above 30°C and the evaporative demand greatly exceeded the amount of precipitation entering the ecosystem during a year.

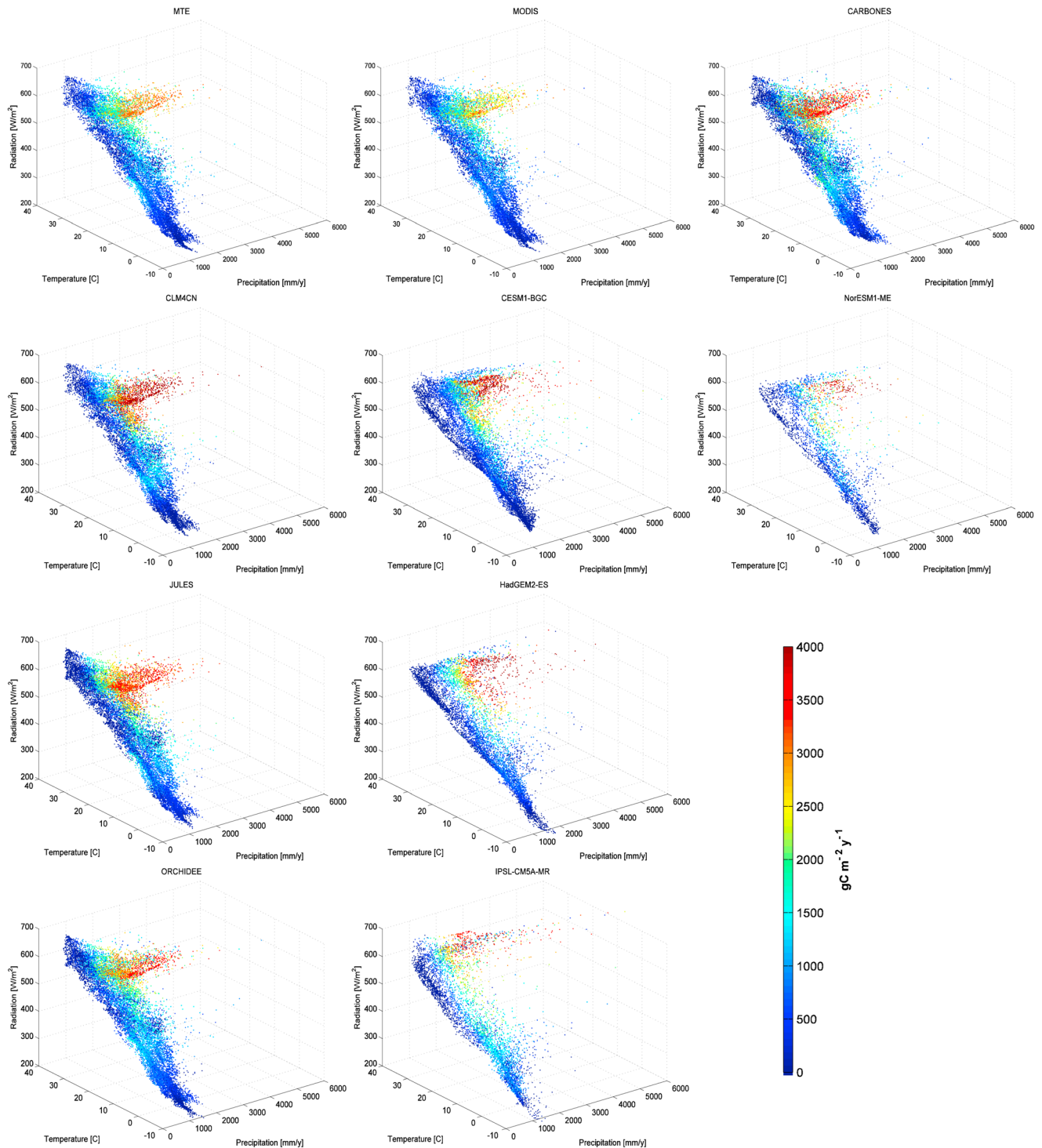


Figure 3. Annual global gross primary production in climate space, represented by mean annual temperature ($^{\circ}\text{C}$), precipitation (mm/yr), and radiation (W/m^2). Each data point represents one grid cell.

In contrast, the highest productivity occurred in areas with high precipitation ($>2000 \text{ mm}/\text{yr}$), moderate temperatures (ranging from 20 to 30°C) and radiation ($500\text{--}600 \text{ W}/\text{m}^2$). These regions correspond to the Intertropical Convergence Zone (ITCZ) characterized by high values in precipitation and moderate radiation due to the cloud cover.

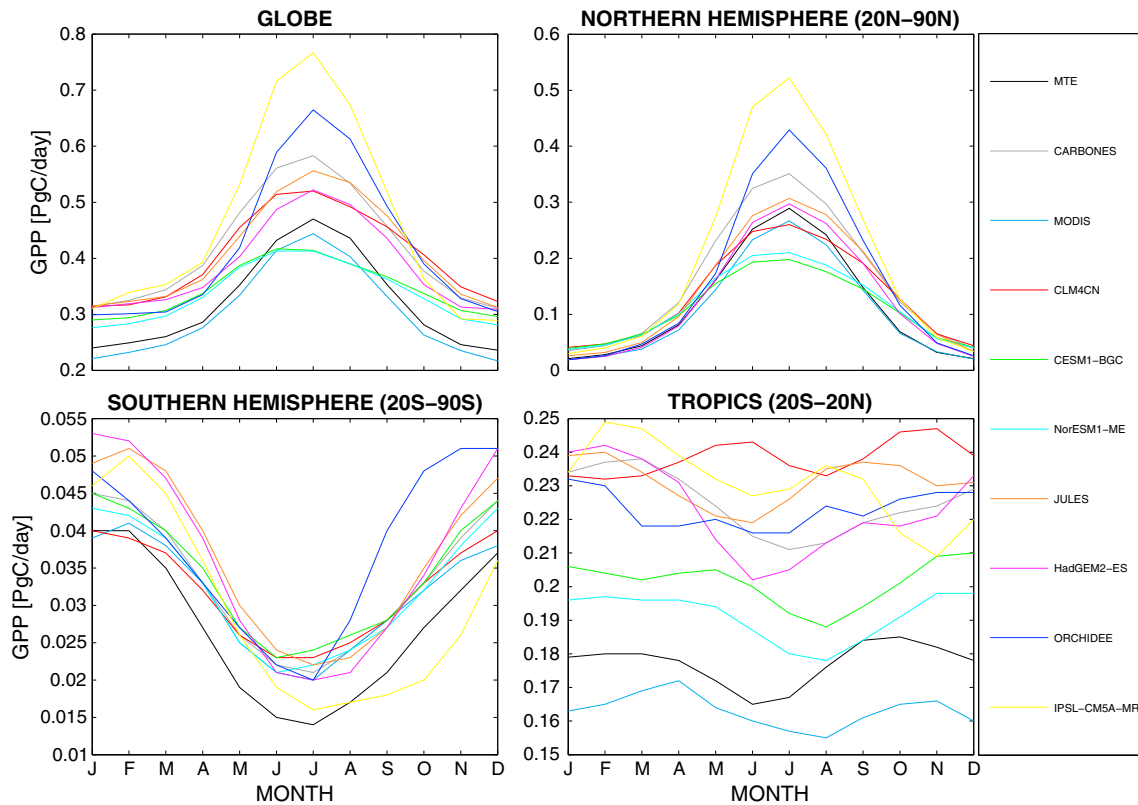


Figure 4. Comparison of seasonal variations in gross primary production among the different data sets.

3.2. Mean Seasonal Cycle

In Figure 4 we compare the mean seasonal cycle of GPP. However, it is difficult to assess the seasonal cycles of the data sets globally given the opposite phase of GPP between hemispheres. Consequently, in the following analysis we show the temporal evolution of GPP over four subdomains (or latitudinal bands).

At the global scale, all data sets show the same seasonal variations, with only CESM1-BGC and NorESM1-ME having a flatter evolution during the boreal summer (Figure 4). Compared to the other data sets, these two ESMs show a lower amplitude in the Northern Hemisphere, and globally their GPPs are virtually the same during the boreal summer. This can be caused by the combined effect of a cold bias in the surface temperature (not shown), nitrogen limitation, and sparse coverage over the boreal arctic zone (Figure 1). However, the zonal averages (Figure 2) suggest that also, CLM4CN has a dip in GPP above 55°–60°N; thus, we can exclude that this drop is caused by a cold bias simulated by the atmospheric components of these two ESMs.

Over the Northern Hemisphere, characterized by a strong seasonality, all the data sets have a GPP minimum during the boreal winter and fall, and a maximum during summer following the spring leaf out. Compared to other data and models, the three data set based on ORCHIDEE (i.e., IPSL-CM5A-MR, ORCHIDEE, and CARBONES) have the largest GPP peaks during the boreal summer. As previously discussed, the large GPP found in IPSL-CM5A-MR is due to the warm bias in surface temperature over the high latitudes of Northern Hemisphere. In the case of CARBONES and ORCHIDEE, the large GPP peaks are supported neither by a temperature bias nor by an earlier greening-up. This suggests that in this model the water stress is not strong enough during the peak growing season [Anav et al., 2011]. In the Southern Hemisphere all the data sets reproduce the phase of the winter GPP minimum, with MTE being lower than the other data. A large spread is found in the tropical regions; however, this domain is characterized by a low seasonality.

Figure 5 shows the errors of each of the selected GPP data set in reproducing the seasonal cycle compared to a reference data set. In the Taylor diagram (i.e., Figure 5), the GPP standard deviation simulated by a given model is proportional to the radial distance from the origin, while the radial distance from the reference

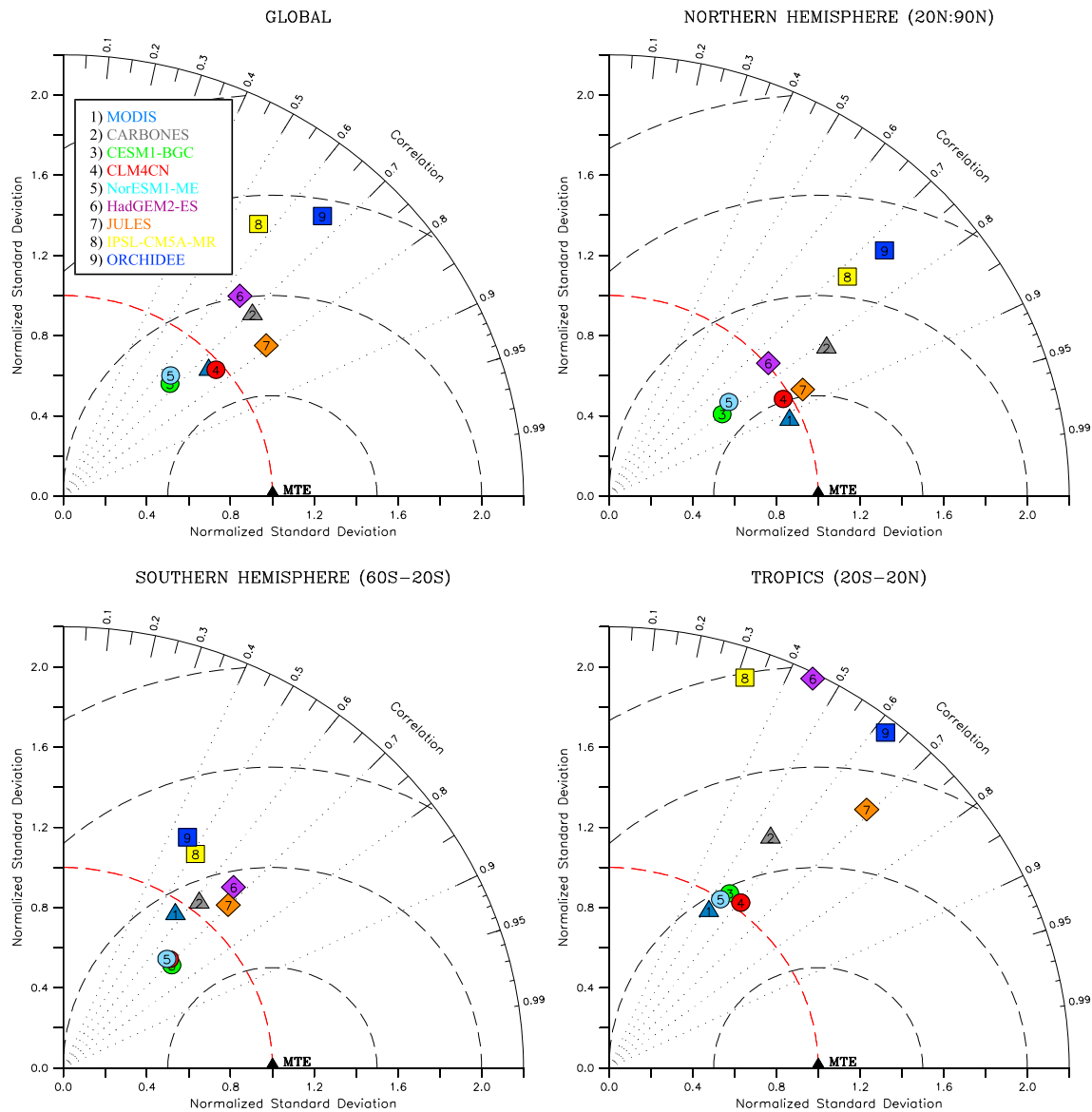


Figure 5. Taylor diagram for the 1990–2009 climatological GPP (MODIS refers to the period 2000–2005). Models with the same land carbon scheme are highlighted with the same symbol (triangles for observation-based and hybrid data, squares for models based on ORCHIDEE, diamonds for those based on JULES, and circles for models based on CLM). Dotted lines indicate the correlation, while dashed lines represent the root mean standard error.

point along a horizontal line is proportional to the root-mean-square difference [Taylor, 2001]. Thus, these statistics can be used to highlight how much of the overall root-mean-square difference (RMSD) is related to differences in amplitude and how much is due to the differences in the phase between models and observation-based data. A model in perfect agreement with the reference data would be located where the circle with radius equal to unity intersects the x axis.

In this plot we chose as reference the MTE, since it falls in the middle of the observation-based (MODIS) and hybrid (CARBONES) data range (Figure 4). It should also be noted that, although MTE cannot be regarded as a “pure” observational data set, it has been widely used to compare or validate different models [e.g., Frankenberg *et al.*, 2011; Anav *et al.*, 2013; Piao *et al.*, 2013; Barman *et al.*, 2014; Guanter *et al.*, 2014; Traore *et al.*, 2014].

The reference GPP is represented in the plots by a black triangle on the x axis (zero correlation error) at unit distance from the origin (no error in standard deviation). The other data-driven data sets (i.e., MODIS and CARBONES) are represented as a light blue and gray triangle, respectively, and these are compared against

MTE and other models. The models with the same land component are represented with the same symbols. For models MTE and CARBONES, the seasonal cycle has been computed over the period 1990–2009, while we present the seasonal cycle for MODIS over the period 2000–2009 due to the unavailability of data before the 2000.

Consistent with previous results, MODIS, CARBONES, and MTE do not completely agree on the phase of the GPP seasonal cycle, the temporal correlation being slightly higher than 0.7 for both MODIS and CARBONES at global scale. A good agreement between the data sets is found in the Northern Hemisphere where MODIS and CARBONES have a correlation above 0.9 and 0.8, respectively. In contrast, there is a poor agreement in the regions characterized by small seasonal amplitudes (i.e., Tropics and Southern temperate areas) where the correlation ranges between 0.5 and 0.6. Considering MODIS, the amplitude ratio (represented by the ratio of standard deviations) typically centers around 1 indicating that the pattern variations are of the right amplitude with respect to MTE. In contrast, CARBONES systematically shows a normalized standard deviation above 1, suggesting a larger seasonal cycle compared to MTE.

The models display a complex pattern, but three important conclusions can be easily drawn looking at Figure 5. First, the climate-biased ESMs are closer to their equivalent offline models than to each other, indicating that the parameterization of GPP is more important for controlling the seasonal phase of GPP than the climate used to drive each land carbon model. In fact, in most of the regions, we can clearly see that pairs of coupled and uncoupled models using the same land component are closer than models having different land components; namely, HadGEM2-ES and JULES have similar skills, as do CLM4CN, CESM1-BGC, and NorESM1-ME, and ORCHIDEE with IPSL-CM5A-MR.

Second, in all the regions the error of the offline models is smaller than the RMSD of the equivalent online models. This likely depends on the bias in the simulated climate that affects the results and performances of the online carbon models. These results are consistent with *Dalmonech et al.* [2015] who compared the Earth system model Max Planck Institute-ESM with its offline land component finding that the bias in climate does not affect the phenology and seasonal carbon fluxes, but it significantly controls the magnitude of GPP.

Third, neither the observation-based product (MODIS) nor the hybrid data set (CARBONES) are better than the process-based models.

Finally, although CARBONES is based on an optimized version of ORCHIDEE, it has skills closer to HadGEM2-ES and JULES rather than to ORCHIDEE, indicating how the data assimilation significantly has improved the performances of ORCHIDEE.

Considering the models' performances, at global scale JULES shows the lowest RMSD and the highest seasonal correlation compared to MTE, with CLM4CN, CESM1-BGC, and NorESM1-ME having similar skills, although CESM1-BGC and NorESM1-ME have a lower correlation and a weaker seasonal cycle compared to CLM4CN and the reference data (MTE). The largest mismatch is found in ORCHIDEE and IPSL-CM5A-MR both having the highest RMSD and standard deviations with the lowest correlations.

In the Northern Hemisphere, characterized by large GPPs during the boreal summer, all the models, except ORCHIDEE, IPSL-CM5A-MR, and HadGEM2-ES, have a correlation above 0.8. JULES and CLM4CN have a good agreement with MTE, given their low RMSDs and normalized standard deviations close to the unit distance from the origin. In contrast, the ESMs based on CLM4CN show large errors explained by the small amplitude in the seasonal cycle.

In the Southern Hemisphere, clearly models with the same land component are clustered near each other, while in the Tropics, characterized by low seasonal amplitude, models are more scattered in comparison to the other subdomains. CLM4CN, CESM1-BGC, and NorESM1-ME have perfect amplitude, the ratio of standard deviation being 1, while all the other models show larger seasonal amplitudes.

3.3. Interannual Variability

The ability of a climate model to capture realistic interannual variability is an important measure of its performance. Here we use the standard deviation of annual values simulated over the 1990–2009 to indicate the magnitude of the model's interannual variability. For comparison, MODIS data for the years 2000–2009 are also presented.

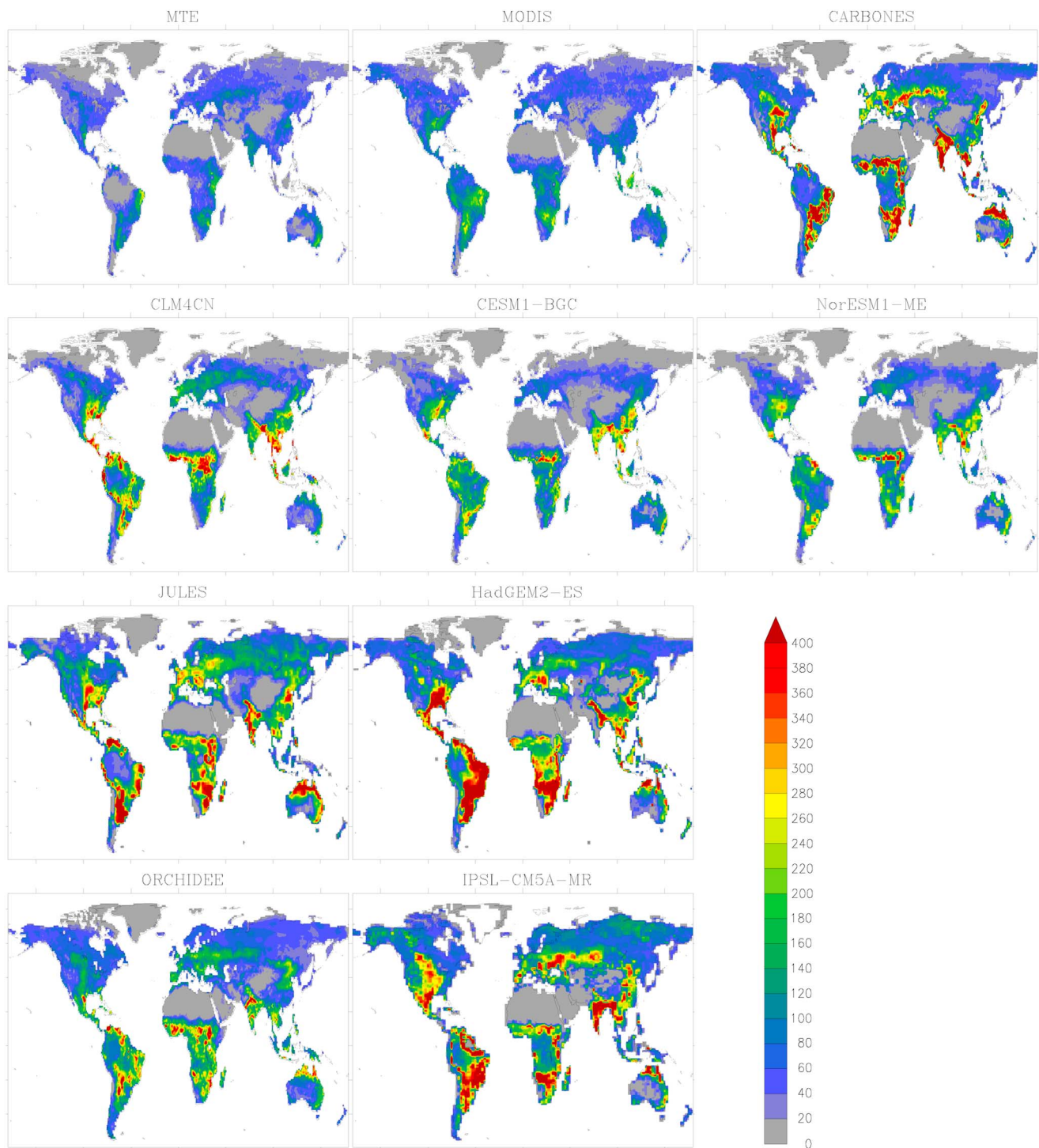


Figure 6. Spatial distribution of GPP interannual variability ($\text{g C m}^{-2} \text{yr}^{-1}$) computed over the period 1990–2009 as simulated by CMIP5 and TRENDY models and compared to reference data (MTE and MODIS) and a hybrid data set (CARBONES).

Looking at the spatial pattern of the interannual variability of GPP (Figure 6), there is a clear difference between CARBONES, MTE, and MODIS, with the latter two showing a weaker variability than CARBONES, only partially explained by the lower annual mean (Figure 1). Regarding MTE, as discussed by *Jung et al.* [2009] and *Piao et al.* [2013] it should not be used as benchmark for interannual variability (IAV).

In fact, there are different reasons why the interannual variability is weakly reproduced by MTE: first, the magnitude of the year-to-year variability is smaller than the spatial and seasonal variability, suggesting that this small variance is partially neglected during the model tree training [Jung *et al.*, 2009]. Second, the factors controlling the spatial GPP gradients may differ between different years [Reichstein *et al.*, 2007]. In other words, the MTE-GPP is trained by spatial gradients among different sites, and then it uses the derived relationship to extrapolate to temporal interannual gradients. This assumes that the GPP spatial and interannual sensitivity to climate variation are the same during all the years, which may be not correct [Piao *et al.*, 2013]. Finally, the controlling factors for the spatial GPP, calculated from satellite fAPAR and climate predictors, might be not very reliable due to clouds that affect satellite retrieval.

In contrast, based on the ability of MODIS NPP in capturing drought effects [Zhao and Running, 2010], it is difficult to conclude that there is an issue in the low IAV of MODIS. Thus, one possible explanation for the lower correlation of MODIS GPP to CO₂ annual growth rate than NPP lies in the fact that autotrophic respiration is also an important carbon emission cost for vegetation to survive and finally fix carbon as biomass, and environmentally, it is largely controlled by temperature [Tjoelker *et al.*, 2001; Clark *et al.*, 2003; Zhao and Running, 2011].

The IAV simulated by all the models is more similar to CARBONES than to MTE or MODIS, although some significant local to regional differences exist between the models. IPSL-CM5A-MR shows the same spatial pattern and magnitude of the year-to-year variability as CARBONES, while ORCHIDEE reproduces the same spatial pattern but with a lower magnitude in the variability. JULES also has the same pattern as CARBONES, while HadGEM2-ES has a higher IAV in Central and South America and a lower IAV over India. Finally, CLM4CN, CESM1-BGC, and NorESM1-ME have a weaker magnitude in the IAV when compared to other models and CARBONES, but the spatial pattern is in agreement with results from other data sets.

All the different data sets assume that the main climatic forcings controlling the GPP are the surface air temperature, the incident solar radiation, and the soil water availability, the latter being strongly related to precipitation (see Appendix A). Figure 7 shows the spatial distribution of climatic controls on the interannual variability of GPP over the period 1990–2009 (2000–2009 for MODIS). The variability caused by each climatic factor (i.e., temperature, radiation, and precipitation) is assessed through the square of temporal correlation coefficients between GPP fluxes derived from the models' simulations and the input data used to force each model. For MODIS, MTE, and CARBONES, we used CRU-NCEP as climate drivers. While the latter two data sets use CRU to estimate the GPP, MODIS is trained by DOE II reanalysis; however, Zhao and Running [2010] reported small discrepancies between CRU and DOE data.

Figure 7 shows that in the offline models the interannual variability of GPP over high latitudes and around the Tibetan plateau (i.e., in the cold regions) is mainly explained by temperature changes, while precipitation variations are the major driving variable in most of other regions, except western Amazonian forests where the contributions from the radiation is also significant. In contrast, in all the ESMs temperature and radiation tend to be colimiting in the high latitudes of the Northern Hemisphere. Consistent with the TRENDY models, precipitation is the main driving variable controlling the GPP variability at global scale.

Previous studies suggest that at high latitudes temperature controls the year-to-year GPP variability, since boreal and arctic ecosystems are cold and rarely water limited [Churkina and Running, 1998; Nemani *et al.*, 2003; Piao *et al.*, 2009]. However, our results suggest that offline models display temperature as the main limiting factor in the cold regions of the Northern Hemisphere, while ESMs give a more important role to radiation. This is explained by the coupling between the atmosphere and the underlying land surface, i.e., high temporal consistency between the atmosphere and the land surface. In fact, while in the offline models, the forcing input are prescribed and the surface fluxes do not modify the planetary boundary layer or forcing data; in the online models the surface climate is the result of the feedbacks between the lower troposphere and the underlying vegetation and soil. In other words, in the online models the surface air temperature depends on the surface energy balance:

$$\frac{\partial E_s}{\partial t} = R_s - LE - SH \quad (1)$$

where $\partial E_s / \partial t$ indicates the variation in time of the energy content of the soil, R_s is the net surface radiation defined as the sum of short- and long-wave contributions, and LE and SH refer to latent and sensible

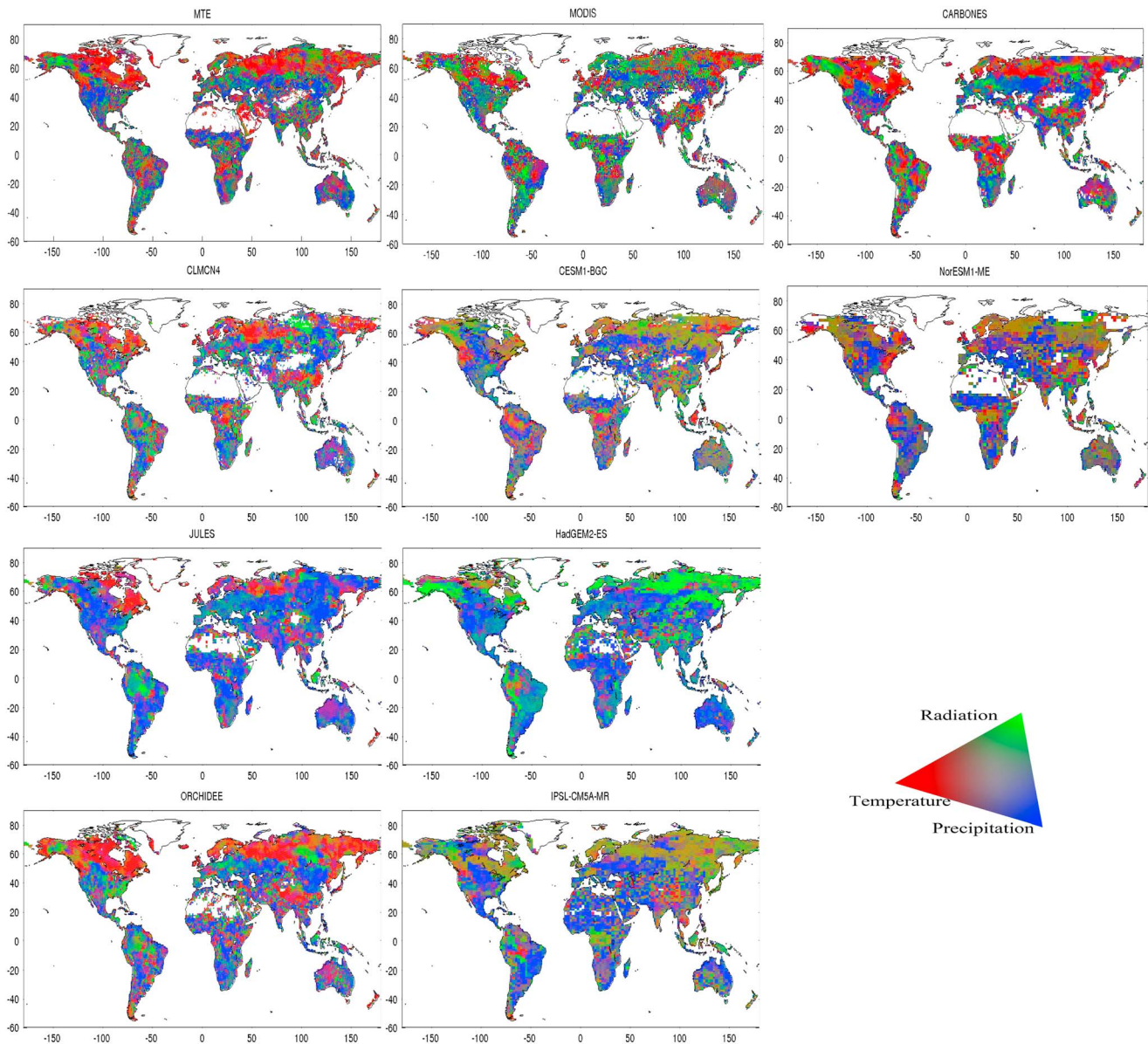


Figure 7. Spatial distribution of climatic controls on interannual variation of GPP.

fluxes, respectively. This equation suggests that the surface air temperature strongly depends on the radiation; thus, radiation and temperature covariate in time, resulting in a covariation for the GPP.

3.4. Trend

Linear GPP trends over 1990–2009 (2000–2009 for MODIS) were computed for each grid point using linear regression analysis; the spatial patterns of these trends are mapped in Figure 8. In general, all the data sets predict an increase of GPP over time; this positive trend is due to a positive response of plant production to both increasing CO₂ concentration and surface temperature. Nevertheless, there are some areas with negative trends in GPP likely explained by decreasing precipitation or large-scale droughts [Zhao and Running, 2010; Zscheischler et al., 2014] or by increasingly intense dry seasons.

The weakest trends are found in MTE and MODIS, and this likely depends on the lack of the fertilization effect due to increasing CO₂. In fact, atmospheric CO₂ rose from about 340–390 ppm during our study period, but neither MTE nor MODIS take into account the rising CO₂ level in their algorithms.

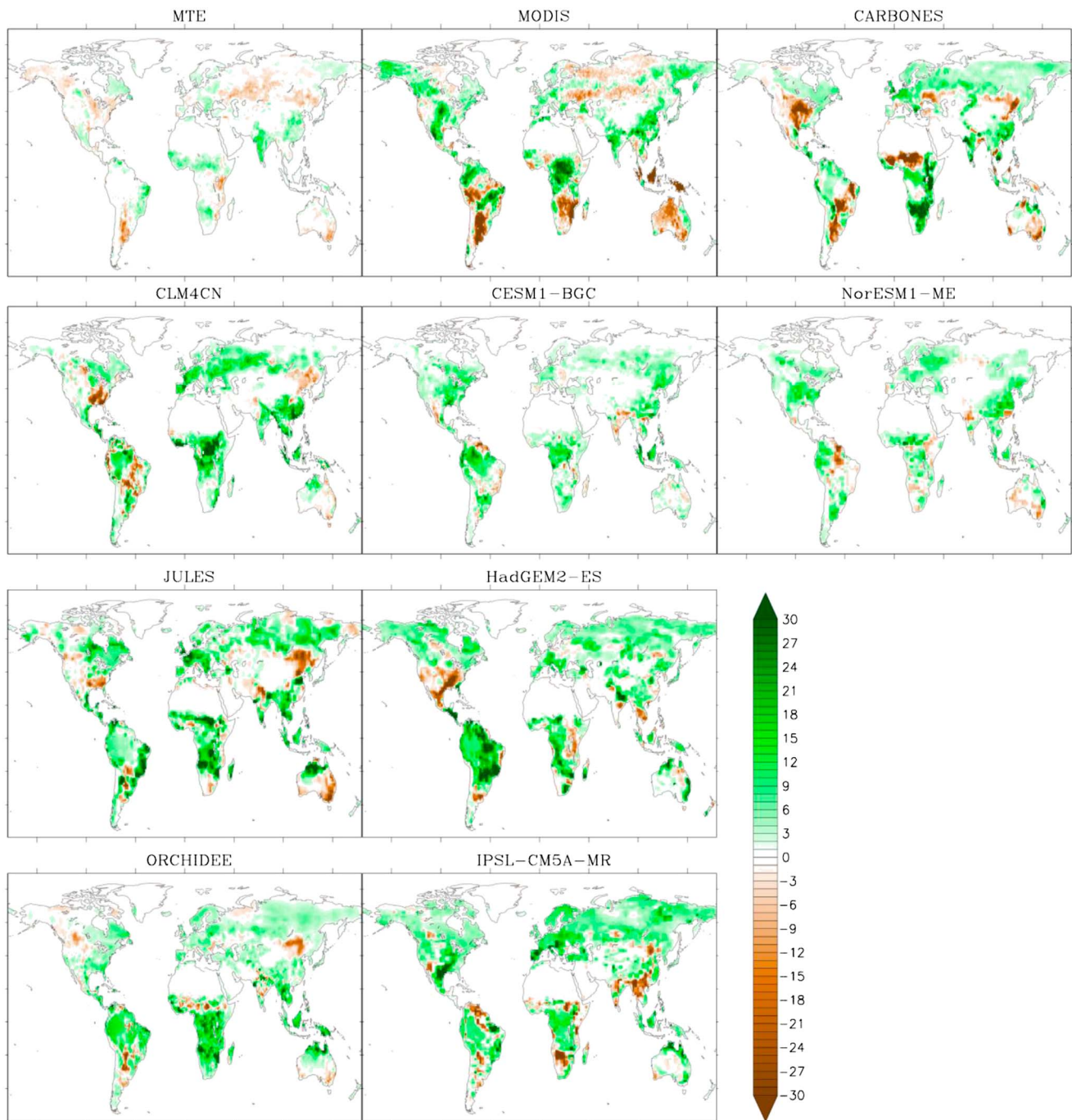


Figure 8. Spatial distribution of GPP trends ($\text{g C m}^{-2} \text{yr}^{-2}$) from 1990 to 2009. Green areas indicate increasing GPP, and brown areas indicate decreasing GPP.

Coupled models have similar trends as their corresponding offline versions, indicating that the trends of climatic forcing are well simulated by the ESMs. In addition, since for process models trends are primarily due to CO_2 fertilization, the similar trends in online and offline simulations are the direct consequence of the same atmospheric CO_2 forcing.

In general, models, observation-based data, and the hybrid data set show large areas with increased GPP over the Northern Hemisphere (Figure 8) mainly due to lengthening of the growing seasons by warming and wetter climate that enhances plant growth [Piao *et al.*, 2007; Zhao and Running, 2010; Murray-Tortarolo

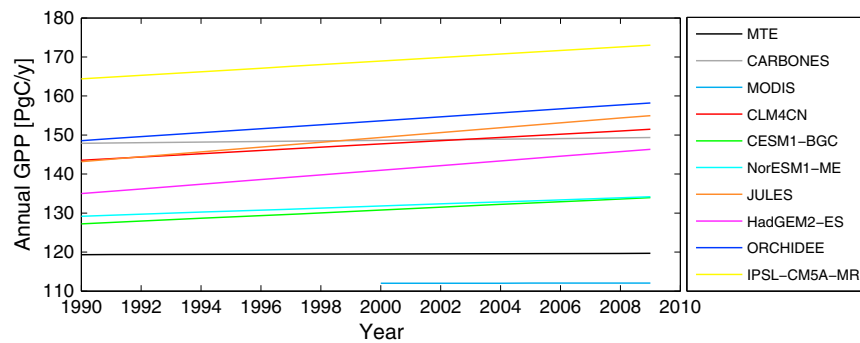


Figure 9. Global GPP trends for different data sets computed using the linear regression analysis.

et al., 2013]. However, continued warming may offset these benefits of an earlier spring and decrease carbon sequestration in a dryer summer and warmer autumn, which could explain the negative trend found in some areas of Northern Hemisphere [Piao et al., 2014].

The models simulate a large positive trend in the Southern Hemisphere, with the exception of a few isolated areas. In contrast, MODIS shows large regions with a negative trend. Zhao and Running [2010] suggested that despite the increased precipitation, the warming trend induced a much higher evaporative demand, leading to a drying trend. As a result, MODIS reports decreasing NPP because of warming-associated drying trends. Vegetation indices from satellite data also showed reduction of greenness over the Southern Hemisphere from 2000 to 2009 [Gobron et al., 2010; Zhao and Running, 2011]. The reduced greenness is in line with the reduced soil moisture derived from satellite data in the same data period [Jung et al., 2010]. However, this effect is not shown here with most of the models simulating an increasing GPP over time. There are large differences in the calculations of GPP between the models and MODIS, namely, for MODIS trends are computed over one decade, while in case of the other data sets trends are computed over two decades. A second reason may lie in the differences in the model structure and parameterization. In fact, the GPP parameterizations are more complex in models than in MODIS (see Appendix A). Thus, we hypothesize three possible mechanisms for this difference: (1) the disturbances (e.g., fires, wind throw, insects' outbreaks, storms, pollution, and human management) are well captured by satellite retrievals and still poorly simulated by models; (2) in the models the CO₂ fertilization effect on stomatal closure is too strong,

Table 2. Site Codes and Names, Dominant Vegetation Types, Locations, Countries, and Main References of the Eddy Covariance Sites Used in This Study^a

Site Code	Site Name	Ecosystem	Latitude	Longitude	Country	Reference
BE-VIE	Vielsam	MF	50.3	5.99	Belgium	Aubinet et al. [2001]
CH-DAV	Davos	ENF	46.81	9.85	Switzerland	Churakova et al. [2014]
CZ-BK1	Bily Kriz forest	ENF	49.5	18.54	Czech Republic	Acosta et al. [2013]
DE-HAI	Hainich	DBF	51.07	10.45	Germany	Knohl et al. [2003]
DE-THA	Tharandt	ENF	50.96	13.56	Germany	Grünwald and Bernhofer [2007]
DK-SOR	Soroe	DBF	55.48	11.64	Denmark	Pilegaard et al. [2001]
ES-ES1	El Saler	ENF	39.34	-0.31	Spain	NA
FI-HYY	Hyytiälä	ENF	61.84	24.29	Finland	Suni et al. [2003a]
FI-SOD	Sodankylä	ENF	67.36	26.63	Finland	Suni et al. [2003b]
FR-HES	Hesse	DBF	48.67	7.06	France	Granire et al. [2000]
FR-LBR	Le Bray	ENF	44.71	-0.76	France	Berbigier et al. [2001]
FR-PUE	Puechabon	EBF	43.74	3.59	France	Rambal et al. [2004]
IT-REN	Renon	ENF	46.58	11.43	Italy	Montagnani et al. [2009]
NL-LOO	Loobos	ENF	52.16	5.74	Netherland	Dolman et al. [2002]
US-HA1	Harvard forest	DBF	42.53	-72.17	USA	Urbanski et al. [2007]
US-HO1	Howland forest	ENF	45.20	-68.74	USA	Hollinger et al. [1999]

^aThe vegetation types are evergreen needleleaf forests (ENF), evergreen broadleaf forests (EBF), deciduous broadleaf forests (DBF), and mixed forests (MF). NA, not available.

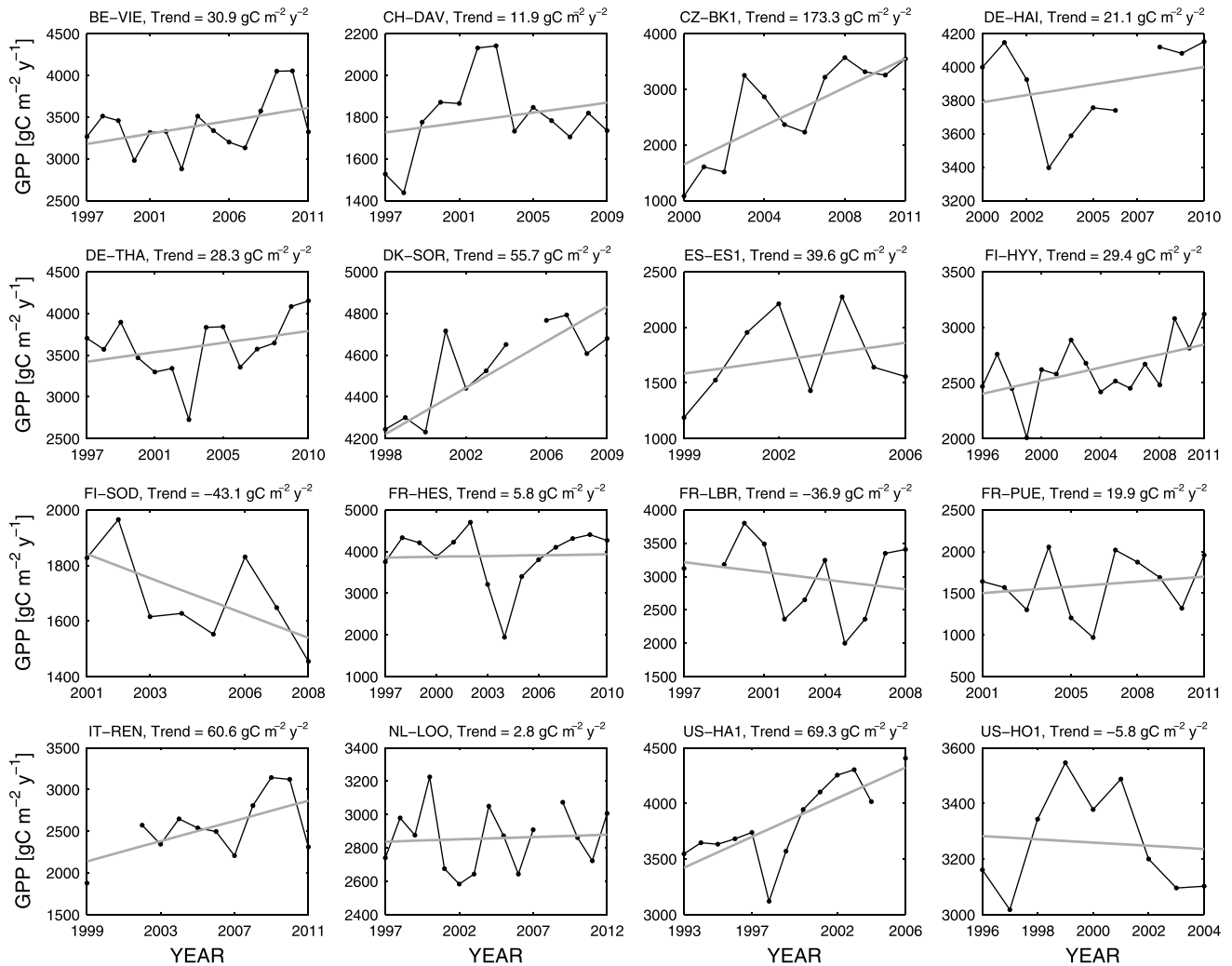


Figure 10. Temporal GPP trends computed over different eddy-towers measurement stations for the period JJA (June–August) (see Table 2).

leading to vegetation with high resistance to drought; and (3) difference in the time periods (two decades for models versus one decade for MODIS) when calculating the trends. To test the latter case, we have computed for all the data sets the trends over the last 10 years of our reference period (not shown); with the shortened temporal period, models are much closer to MODIS, suggesting that the CO₂ effect is reduced by recent climate variability (i.e., drought or extreme events).

Looking at the mean annual global values (Figure 9), all the models have an increasing trend, while both the observation-based data sets and the hybrid data show near-zero or slightly positive trends (CARBONES 0.08 Pg C yr⁻², MTE 0.018 Pg C yr⁻², and MODIS 0.005 Pg C yr⁻²). Considering the observation-based data and CARBONES, the lack of relevant positive trend can be explained by a compensation of points with a negative and a positive trend (Figure 8).

The CLM-based models have the smallest positive trends in GPP. CLM4CN is the only model in this study that takes into account nitrogen limitation when computing photosynthesis (Table 1). This suggests that in some ecosystems, the potential CO₂ fertilization effect may already be strongly limited by present-day nitrogen availability [Vitousek and Howarth, 1991]. This result is consistent with Sitch *et al.* [2015] who have analyzed the net primary production trends simulated by nine different DGVMs (Dynamic Global Vegetation Models) finding that models with a fully coupled carbon and nitrogen cycle simulate a flatter increase in the land sink. This conclusion is also supported by results from coupled models: among all the ESMs, those based on CLM4CN have the weakest trend (CESM1-BGC 0.35 Pg C yr⁻² and NorESM1-ME 0.26 Pg C yr⁻²).

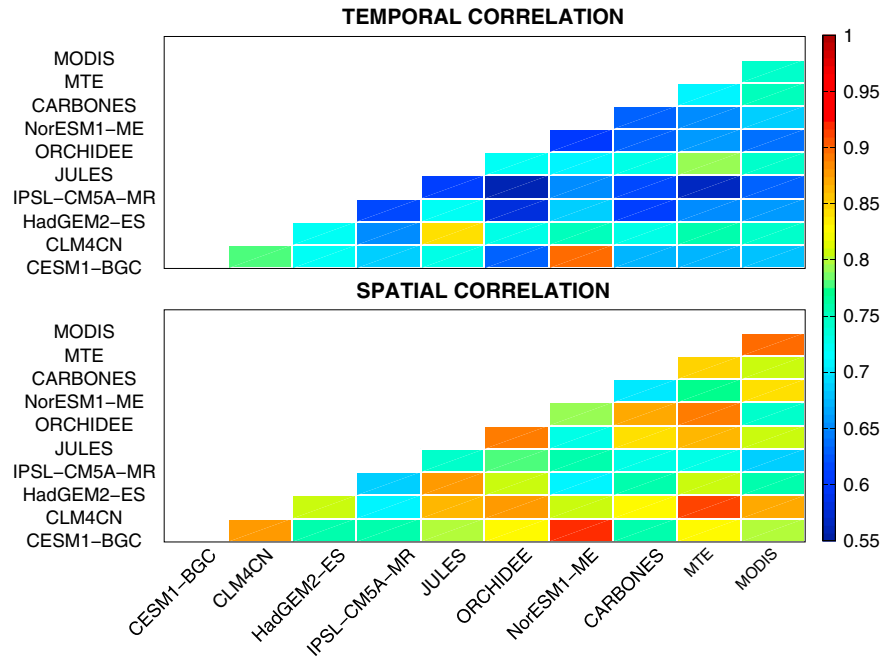


Figure 11. (top) Temporal and (bottom) spatial cross correlation computed between different carbon models and data-driven GPP estimates. The temporal correlation has been computed using the 1990–2009 climatological mean (2000–2009 for MODIS), while the spatial correlation is based on a pointwise correlation of the long-term annual means.

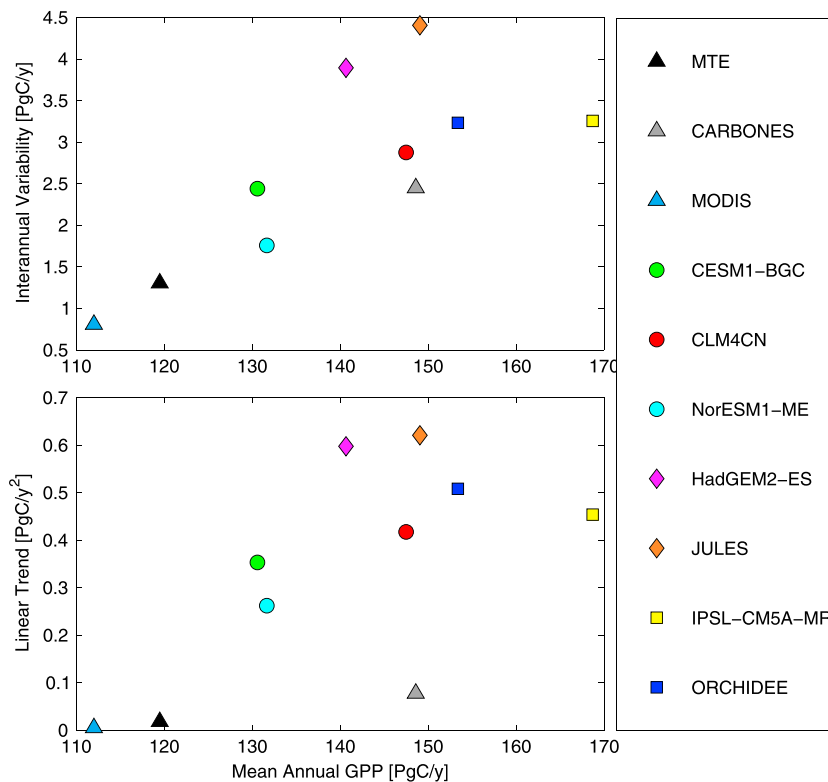


Figure 12. Integrated mean annual GPP (*x* axis) with its (top) IAV (*y* axis) and (bottom) trend (*y* axis) as simulated by CMIP5 and TRENDY models, observation-based data (MTE and MODIS), and a hybrid data set (CARBONES).

Table 3. Synthesis of Global Mean Annual GPP, Interannual Variability, and Trend

Data Set	Mean (Pg C yr ⁻¹)	IAV (Pg C yr ⁻¹)	Trend (Pg C yr ⁻²)
MTE	119	1.3	0.0181
MODIS	112	0.8	0.005
CARBONES	148	2.45	0.078
CLM4CN	147	2.87	0.417
CESM1-BGC	130	2.44	0.353
NorESM1-ME	131	1.76	0.262
JULES	149	4.4	0.621
HadGEM2-ES	140	3.89	0.598
ORCHIDEE	153	3.23	0.508
IPSL-CM5A-MR	169	3.26	0.454

Conversely, models that do not reproduce the nitrogen limitation might overestimate the CO₂ fertilization, leading to high GPP trends (e.g., JULES 0.62 Pg C yr⁻² and HadGEM2-ES 0.6 Pg C yr⁻²).

It is well recognized that the MTE should not be used as a benchmark for trends [Jung et al., 2009; Anav et al., 2013; Piao et al., 2013]. However, since it relies on flux tower local observations,

one could argue whether eddy covariance data capture any trend in GPP and thus attribute the lack of trends in MTE to the missing CO₂ fertilization. To test this hypothesis, as well as to check if model and data trends are consistent in their long-term trend, we selected 16 eddy covariance sites with a long enough record (Table 2). Because of the lack (or poor quality) of data during winter for many sites and years, we compute the trends only over the period June–August (JJA), i.e., during the most productive periods of the growing season. The relatively short time series of the sites (8–10 years), the strong impact of interannual variability and extreme events (e.g., 2003 heat wave [Ciais et al., 2005] with its lag effects [Granier et al., 2007]), the effects of possible local disturbance and management practices, and changes in the measurement systems all make the use

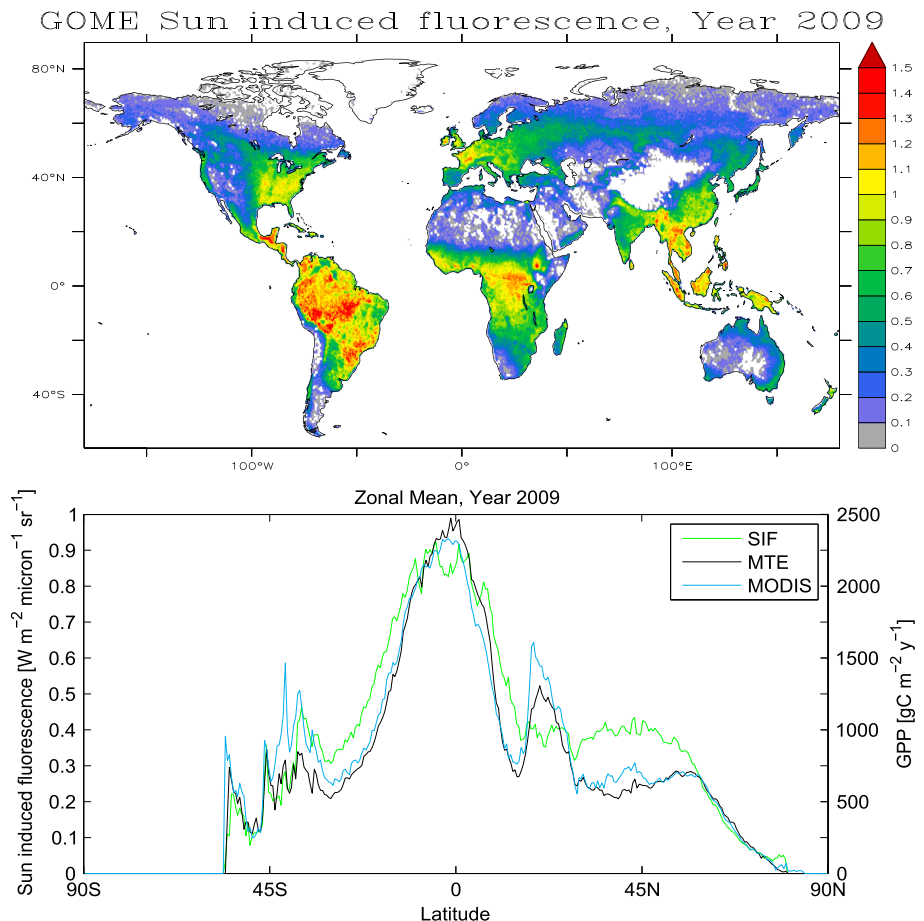


Figure 13. (top) Spatial distribution of 2009 mean annual retrieved chlorophyll *a* fluorescence at 755 nm, and (bottom) comparison of Sun-induced fluorescence and GPP zonal means from different observation-based data sets.

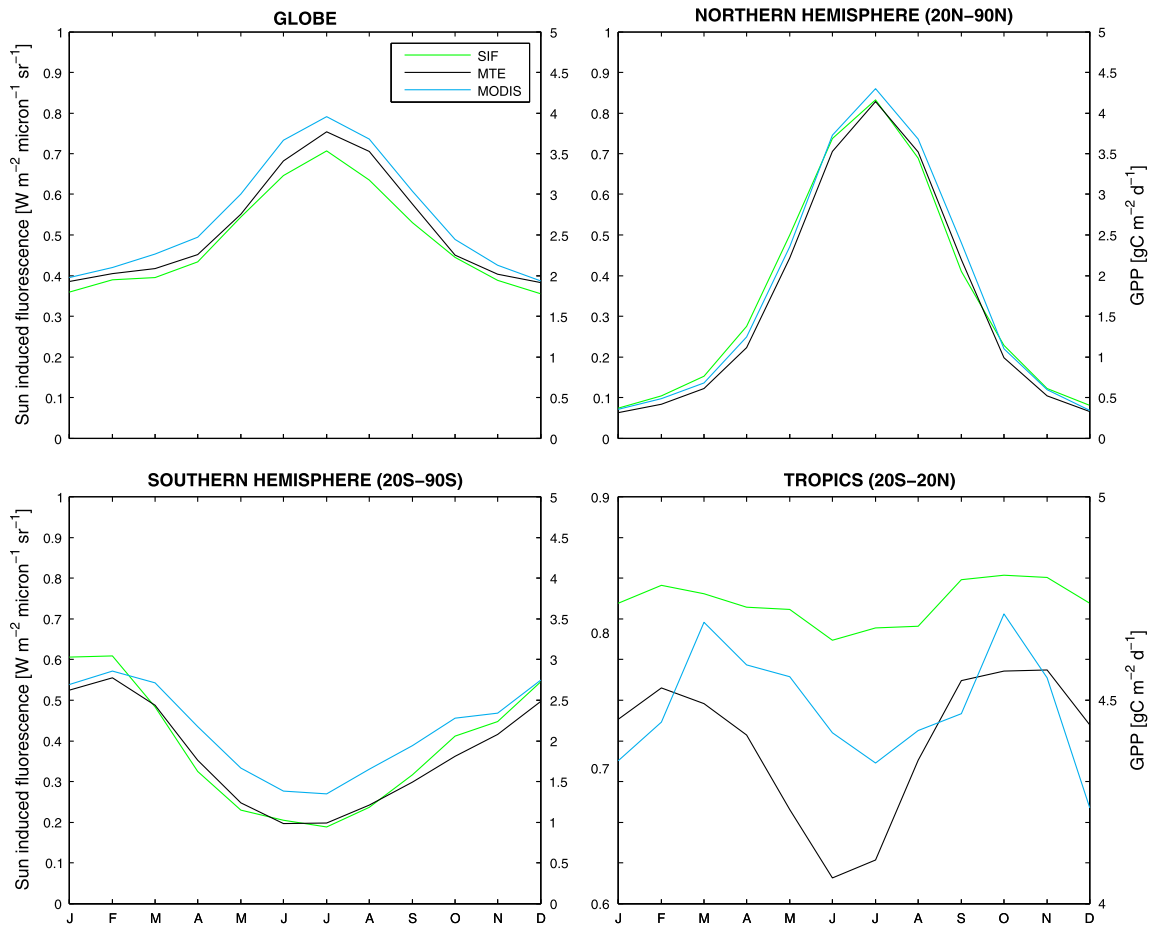


Figure 14. Comparison of Sun-induced fluorescence and gross primary production seasonal cycles for the year 2009.

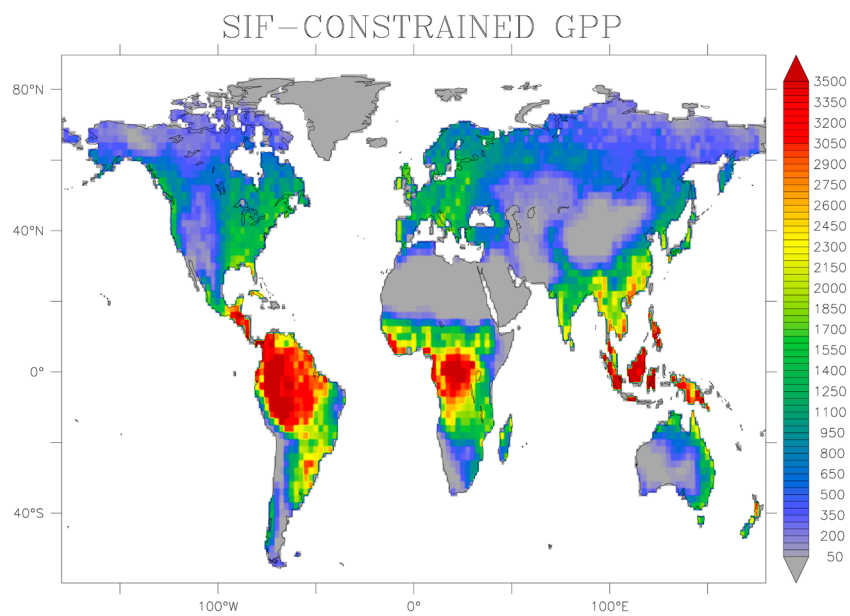


Figure 15. Spatial distribution of mean annual GPP ($\text{gC m}^{-2} \text{yr}^{-1}$) for the year 2010 based on the optimal combination of TRENDY models and GOSAT SIF [see Parazoo et al., 2014].

Table 4. Summary of Advantages and Disadvantages of Different Methods Used to Estimate GPP

	PRODUCTS	ADVANTAGES	DISADVANTAGES
D A T A	MODIS	<ul style="list-style-type: none"> – High spatial coverage – Detects disturbances 	<ul style="list-style-type: none"> – Filling data gaps caused by cloudiness contains uncertainties – Coarse resolution of meteorological input data
	MTE	<ul style="list-style-type: none"> – Well constrained in NH – Climate representativeness 	<ul style="list-style-type: none"> – Coverage of station data – Geographical representativeness – No capacity of extrapolating to completely different conditions – CO₂ fertilization not accounted – Disturbances not accounted
M O D E L S	LAND CARBON	<ul style="list-style-type: none"> – Continuous in space and time – High spatial coverage (depending on meteorological input data) 	<ul style="list-style-type: none"> – Assumptions must be done through parameterizations – Few or none disturbances accounted – Lack of feedbacks with atmosphere
	EARTH SYSTEM	<ul style="list-style-type: none"> – Continuous in space and time – High temporal consistency between atmosphere and land surface 	<ul style="list-style-type: none"> – Assumptions must be done through parameterizations – Few or none disturbances accounted – Bias in climate forcing – Coarser resolution than offline models
H Y B R I D	CARBONES	<ul style="list-style-type: none"> – Well constrained in NH – Climate representativeness 	<ul style="list-style-type: none"> – Coverage of station data – Geographical representativeness

of the eddy covariance data complicated. However, there is clear evidence of GPP increase with time at the selected sites (Figure 10), although the increase is only statistically significant at CZ-BK1, DK-SOR, and US-HA1 (95% significance using a Mann-Kendall test).

4. Summary and Discussion

We have compared the spatial and temporal patterns of GPP as simulated by three TRENDY models and four CMIP5-ESMs, having in common the same land component, with different observation-based data sets and a hybrid product.

A synthesis of the main results is reported in Figure 11, which shows the temporal (top) and spatial (bottom) correlations among the different data sets. The temporal correlations were obtained by comparing the mean seasonal cycles. At the global scale, all the pairs of models and data-driven data sets show a correlation coefficient above 0.55. In general, we found higher correlations when comparing models against MTE rather than to MODIS or CARBONES, with the highest value found for JULES. Considering the cross correlations among models, we observe the highest agreement in the phase of seasonal cycle when comparing CESM1-BGC with NorEMS1-ME; this is due to the similarity between these two ESMs and the low sensitivity of simulated GPP to different climatic forcing.

Conversely, the spatial pattern, based on a pointwise correlation of the long-term annual means, is well represented by all models, the correlations being systematically greater than 0.7. Consistent with the temporal correlations, models display the highest values when compared to MTE rather than to MODIS or CARBONES. The highest correlation is found when CLM4CN is compared to MTE, but ORCHIDEE and JULES also have high correlations. It is also noticeable that comparing models with the same land component (i.e., HadGEM2-ES versus JULES) does not lead to a relevant increase in the correlation with respect to MTE.

Figure 11 suggests that comparing models with the data-based products, the correlations are higher in the uncoupled models than in the ESMs. Specifically, irrespective of the reference data set used as benchmark, CLM4CN has a spatial and temporal correlation higher than CESM1-BGC and NorESM1-ME, as does JULES compared to HadGEM2-ES. For ORCHIDEE and IPSL-CM5A-MR this is only true in the case of spatial correlation. This is likely due to biases in the climatic forcing simulated by the ESMs.

Figure 12 summarizes the main finding on global GPP averages with the associated interannual variability and trends. Some conclusions can be easily drawn looking at this figure. First, all of the simulated GPPs are higher than the MTE and MODIS estimates, while the CARBONES GPP falls in the middle of the simulated range. This latter result is partially expected since CARBONES represents an optimized version of ORCHIDEE. Second, consistent with *Piao et al.* [2013], the global GPP estimates simulated by all the models show a large range, varying from a minimum of 130 Pg C yr^{-1} found in CESM1-BGC to a maximum of 169 Pg C yr^{-1} for IPSL-CM5A-MR (Table 3). When comparing TRENDY models with the ESMs using the same terrestrial carbon models, there is a clear mismatch in the GPP global values: JULES simulates about 9 Pg C yr^{-1} more than HadGEM2-ES mainly due to the larger productivity found over Amazonian forest and the temperate regions of Northern Hemisphere (see Figures 1 and 2). CLM4CN predicts about 16 Pg C yr^{-1} more than the corresponding ESMs due to the larger productivity mainly over the Tropics and Central-Eastern Eurasia, while IPSL-CM5A-MR simulates 15 Pg C yr^{-1} more than ORCHIDEE because of the larger GPP over the Eurasian boreal and Arctic regions. In this latter case, the higher productivity of the coupled models with respect of the corresponding offline version is mainly due to the strong warm bias of the atmospheric component [*Dufresne et al.*, 2013].

A large range in GPP estimates is found also in case of the observation-based data sets and the hybrid product (Table 3). This result indicates that there is still a large uncertainty in the GPP benchmark, and it is confirmed by the large discrepancies in published estimates of GPP. Terrestrial GPP has been estimated at about 120 Pg C yr^{-1} based on $\delta^{18}\text{O}$ measurements of atmospheric CO_2 [*Ciais et al.*, 1997]. Using eddy covariance flux data and various diagnostic models, *Beer et al.* [2010] provide an estimate of $123.6 \pm 8 \text{ Pg C yr}^{-1}$ in the period 1998–2005 consistent with result of *Jung et al.* [2009] and *Ciais et al.* [1997]. Some studies, however, suggest that current estimates of global GPP [*Denman et al.*, 2007; *Ciais et al.*, 2013] might be too low and that a best guess of $150\text{--}175 \text{ Pg C yr}^{-1}$ [*Welp et al.*, 2011] or $146 \pm 19 \text{ Pg C yr}^{-1}$ [*Koffi et al.*, 2012] better reflects the observed rapid cycling of CO_2 . However, these latter studies have some limitations: specifically, *Welp et al.* [2011] have used only a limited number of observations and a very simple model for their results that only calculate the gross photosynthesis (i.e., it does not include any respiratory processes). In general, through photorespiration, plants immediately respire away 20–40% of the carbon fixed by photosynthesis [*Chapin et al.*, 2002]; thus, accounting for photorespiration, the *Welp et al.* [2011] GPP would be closer to the current estimates [*Denman et al.*, 2007; *Ciais et al.*, 2013]. In addition, it should also be noted that in their analysis on long-term time series of CO_2 isotopes *Welp et al.* [2011] found a GPP lower bound of approximately of 120 Pg C yr^{-1} a value close to previous estimates [*Ciais et al.*, 1997; *Jung et al.*, 2009; *Beer et al.*, 2010]. However, to retrieve this latter value, they used a C_{cs}/C_a ratio of 0.66 (where C_{cs} is the CO_2 partial pressure in chloroplasts at the site of CO_2 hydration and C_a represents the atmospheric CO_2 partial pressure); since a ratio of ~ 0.7 is typical of ratios of CO_2 in the intercellular air spaces to CO_2 in the atmosphere (C_i/C_a) of C3 vegetation, it can be argued that two things are neglected to retrieve a GPP of 120 Pg C yr^{-1} : first, the relevant contribution of C4 vegetation to global GPP. In fact, C4 plants have a lower C_i/C_a ratio (~ 0.4 [*Farquhar et al.*, 1993]) than C3 plants, and they approximately contribute to 20–25% of global GPP [*Still et al.*, 2003]. Second, the added resistance of diffusion across the mesophyll which makes C_{cs}/C_a less than C_i/C_a [*Welp et al.*, 2011].

Similarly, *Koffi et al.* [2012] were unable to distinguish the best estimate of $146 \pm 19 \text{ Pg C yr}^{-1}$ from a different data assimilation experiment yielding a terrestrial global GPP of 117 Pg C yr^{-1} .

Consistent with the discussion of section 3.3 (as well as Figure 6), MTE and MODIS have the lowest interannual variability, while models are clustered around CARBONES. The observation-based data sets show no trend (MTE and MODIS), while CARBONES has a slight positive trend, although the length of the temporal period is too short for a detailed analysis. All the models report a positive trend ranging from $0.28 \text{ Pg C yr}^{-2}$ (NorESM1-ME) to $0.62 \text{ Pg C yr}^{-2}$ (JULES). It is also noticeable that models with the same land component show similar magnitude in the IAV and temporal trends, as a consequence of GPP response to prescribed CO_2 . This is particularly evident for the two ESMs using CLM4CN as land component (i.e., CESM1-BGC and NorESM1-ME) that are always close to each other in terms of the total amount of GPP, of interannual variability, and of trends. In this case, since the surface air temperature and the land precipitation from these models have different pattern and bias (not shown), this result suggests that using the same land component in the ESMs is more important in controlling the total

amount of carbon fixed by GPP rather than the difference due to the climatic forcing. *Hajima et al.* [2014] found a similar behavior between CESM1-BGC and NorESM1-ME although they used different diagnostics to compare ESMs.

Besides, Figure 11 highlights how offline models have better performance than ESMs, our results also suggest that performances of coupled models are not that far from offline models, adding confidence in the carbon fluxes simulated by models that use an inner climate and increasing their reliability. This result is reinforced by a recent finding that the bias in climate models does not affect the phenology and seasonal carbon fluxes, but it significantly controls the magnitude of GPP [*Dalmonech et al.*, 2015].

Although there is still a large discrepancy among models and observation-based data sets, during the last years great advances have been made in the use of different sources of data to quantify global spatiotemporal patterns of GPP. For example, carbonyl sulfide (COS) uptake could be used as a proxy for GPP, based on the close relationship between seasonal dynamics of COS and CO₂ mole fractions at regional and continental scales and the link between COS and CO₂ uptake at the leaf level [*Blonquist et al.*, 2011; *Asaf et al.*, 2013]. The coupled uptake of carbonyl sulfide and CO₂ by plants could be used to constrain terrestrial GPP by the combination of atmospheric COS measurements with an inversion of the atmospheric transport once the ratio of CO₂ versus COS uptake, the additional COS deposition to soils, and the COS efflux from oceans is more precisely quantified [*Beer et al.*, 2010].

Recently *Joiner et al.* [2011], *Frankenberg et al.* [2011], and *Guanter et al.* [2014] derived plant fluorescence using high spectrally resolved solar Fraunhofer lines from Earth radiance data measured with Greenhouse Gases Observing SATellite (GOSAT) [*Joiner et al.*, 2011; *Ciais et al.*, 2014]. In particular, *Frankenberg et al.* [2011] found that “global space-borne observations of solar-induced chlorophyll exhibit a strong linear correlation with GPP and that the fluorescence emission even without any additional climatic or model information has the same or better predictive skill in estimating GPP as those derived from traditional remotely sensed vegetation indices using ancillary data and model assumptions.”

To quantify the spatial agreement between the observation-based GPP and satellite fluorescence, in Figure 13 we compare the GOME-2 Sun-induced fluorescence (SIF) [*Joiner et al.*, 2013] with MTE and MODIS GPP for the year 2009. On the annual average, we find a strong spatial correlation between fluorescence and MTE (0.9) and MODIS (0.8) GPP, and the SIF spatial pattern (Figure 13, top) is consistent with results in Figure 1, confirming that SIF can be used as a proxy for GPP. The latitudinal distribution of fluorescence agrees well with MTE and MODIS GPP (Figure 13, bottom), with SIF reproducing the high productivity of tropical environments as well as the dip of the dry subtropical areas and the secondary peaks of temperate regions.

In Figure 14 we compare the seasonal cycle of SIF data with MTE and MODIS GPP for the year 2009. In the regions characterized by a strong seasonality, we found a perfect agreement in the phase of seasonal cycle with MTE and MODIS exhibiting a correlation of 0.99; conversely, the correlation is slightly lower when SIF is compared to MTE in the tropics (0.9) and much poorer compared to MODIS (0.49).

These new advances in space-borne retrieval suggest how it is possible to constrain the GPP directly from satellite observations of chlorophyll fluorescence, using the SIF as a proxy for GPP [*Frankenberg et al.*, 2011]. *Zhang et al.* [2014] recently have shown how SIF data can be also used as an indicator of the magnitude and seasonality of maximum carboxylation rate, a key parameter of the Farquar’s model (see Appendix A). Specifically, even though the maximum carboxylation rate varies in space and time as a function of climate, because of the difficulties in measuring it in the field and then to prescribe values on a global scale, terrestrial carbon models make use of fixed values associated to different plant functional types. *Zhang et al.* [2014] demonstrated that using a seasonally varying maximum carboxylation rate improves the GPP performances compared to simulations with fixed carboxylation rate values.

However, it should be noted that to retrieve the GPP from the fluorescence signal, several assumptions must be made, with GPP depending on the measured fluorescence and APAR [*Frankenberg et al.*, 2011; *Guanter et al.*, 2014]. The assumption of a linear relationship between SIF and GPP might be not valid for all the ecosystems or under different light and temperature conditions; thus, the SIF-based GPP should be inferred using biome-specific regressions. This is confirmed by *Guanter et al.* [2012] who showed that the relationship between SIF and GPP is sensitive to vegetation type and climate.

Recently, *Parazoo et al.* [2014] inferred the global distribution of GPP from an ensemble of eight DGVMs constrained by global measurements of SIF from the Greenhouse Gases Observing Satellite (GOSAT). In Figure 15 we show the 2010 annual distribution of GPP obtained with this approach: although here we focus only on a specific year, the spatial pattern is consistent with results of Figure 1 with high annual GPP in the tropics and lower values over dry-cold regions. Also, the global SIF-constrained GPP estimate (144 Pg C yr^{-1}) is closer to models than MTE or MODIS. However, this latter result is somewhat expected since *Parazoo et al.* [2014] used an ensemble mean of eight TRENDY models to convert the SIF signal into GPP.

5. Conclusions

Our results indicate a large range in mean annual GPP estimates with associated large uncertainty in the interannual variability and trends. This result reinforces the well-known problem that a perfect global GPP data set does not exist; in fact, all the data sets analyzed in this paper have some advantages/disadvantages (Table 4). Considering MODIS and MTE, our results indicate that these data sets have some issues on the IAV and trends that need to be addressed in the future. In contrast, because of the wide range in GPP estimates and the large uncertainties in future climate projections [*Friedlingstein et al.*, 2006; *Arora et al.*, 2013], all the models need to be improved since several processes are still missing [*Ciais et al.*, 2013].

For instance, most of the models do not simulate human management including fertilization and irrigation [e.g., *Gervois et al.*, 2008; *Runyan et al.*, 2012], disturbances like fire, logging, harvesting, insect outbreaks, and ecosystem dynamics (migration, variation in forest age and structure, and forest regrowth from abandoned crops fields). In addition, nitrogen dynamics are simulated by only few models (Table 1), although the importance of terrestrial nitrogen-carbon cycle interactions is well known [*Magnani et al.*, 2007; *Zaehle*, 2013], and very few models have phosphorus dynamics (none of the models in this study) [*Zhang et al.*, 2011; *Goll et al.*, 2012]. Also, the impact of tropospheric ozone on photosynthesis is included only in a few models [*Sitch et al.*, 2007; *Anav et al.*, 2011]. Finally, several processes related to the decomposition of soil carbon are poorly simulated or not represented at all [*Todd-Brown et al.*, 2013].

The lack of all these parameterizations within carbon cycle models could result in an overall overestimation of global GPP that might explain the mismatch with the data-driven GPP (i.e., MTE and MODIS). Thus, the priority for developing carbon cycle modeling with processes that current models treat either very simplistically or not at all is imperative in the next future to improve present GPP estimates and better quantify the future uptake of carbon dioxide by the world's vegetation.

However, although one would expect that a model that includes several relevant processes for the carbon cycle should be more realistic than a simpler model, this does not automatically increase its reliability and robustness [*Prentice et al.*, 2014]. In fact, adding more processes to the existing models leads to an increase in models' complexity but also to an increase of the uncertainty associated to the introduction of new model parameters. In particular, increasing the complexity of existing models could lead to models fitting well the observations over the sites where they have been tuned, but they could produce divergent results over areas different from the domain of calibration [*Prentice et al.*, 2014].

This is suggesting also that more long term observations are needed, in particular, in areas currently under represented. The recent development of international research infrastructures such ICOS (www.icos-ri.eu), NEON (www.neoninc.org), and AmeriFlux (<http://ameriflux.lbl.gov>) that are investing in organized and high-quality networks will help to provide more observations for model constrain and validation.

Finally, the new advances in space-borne retrieval suggest how it is possible to constrain the GPP directly from satellite observations of chlorophyll fluorescence, providing therefore a new and reliable tool to improve our knowledge on the global carbon cycle.

Appendix A: Photosynthesis at the Leaf Level

A1. CLM4CN

Following *Collatz et al.* [1991, 1992] and *Oleson et al.* [2010] the leaf photosynthesis (A , $\text{mol m}^{-2} \text{ s}^{-1}$) is estimated as the minimum of three assimilation limited rates: the Rubisco (leaf enzyme) limited rate w_c ,

the light-limited rate w_j , and the carbon compound export limitation (C_3 plants) or PEP-carboxylase limitation (C_4 plants) w_e , namely,

$$A = \min(w_c, w_j, w_e) \quad (A1)$$

The Rubisco-limited rate of carboxylation is ($\text{mol m}^{-2} \text{s}^{-1}$):

$$w_c = \begin{cases} \frac{V_m(c_i - \Gamma_*)}{c_i + K_c \left(1 + \frac{O_i}{K_o}\right)} & \text{for } C_3 \text{ plants} \\ V_m & \text{for } C_4 \text{ plants} \end{cases} \quad (A2)$$

where c_i is the partial pressure of CO_2 in interior leaf (Pa), O_i is the partial pressure of O_2 in interior leaf (Pa), K_c (Pa) is the Rubisco Michaelis-Menten constant for CO_2 ($K_c = 30 \times 2.1^{Q_{10}}$), K_o (Pa) is Rubisco inhibition constant for oxygen O_2 ($K_o = 30000 \times 1.2^{Q_{10}}$), Γ_* (Pa) is the CO_2 compensation point ($\Gamma_* = 0.5 \times O_i / [2600 \times 0.57^{Q_{10}}]$), and V_m is a PFT-dependent value representing the maximum catalytic capacity of Rubisco at saturating levels of Ribulose biphosphate (RuBP) and intercellular partial pressure of CO_2 ($\text{mol m}^{-2} \text{s}^{-1}$), which varies with leaf temperature (T_l) and soil water:

$$V_m = V_{\max} f_T(T_l) f_w(\theta) \quad (A3)$$

where V_{\max} represents the maximum rate of carboxylation of the enzyme Rubisco at 25°C in the presence of saturating soil water, and it is assumed to be a function of leaf nitrogen as over 20% of leaf nitrogen is invested in Rubisco [Dai et al., 2004]. The temperature dependence $f_T(T_l)$ of V_m is calculated as follows:

$$f_T(T_l) = \begin{cases} \frac{2.1^{Q_{10}}}{1 + e^{0.3(T_l - s_2)}} & \text{for } C_3 \\ \frac{2.1^{Q_{10}}}{[1 + e^{0.3(T_l - s_2)}] / [1 + e^{0.2(s_4 - T_l)}]} & \text{for } C_4 \end{cases} \quad (A4)$$

with Q_{10} (unitless) is a temperature coefficient ($Q_{10} = [T_l - 298.16]/10$), s_2 is the high-temperature inhibition parameter (K), and s_4 is the low-temperature inhibition parameter (K).

The effect of soil water stress on assimilation is given by

$$f_w(\theta) = \sum_{i=1}^N r_i \left(\frac{\psi_{\max} - \psi_i}{\psi_{\max} + \psi_{\text{sat},i}} \right) \quad (A5)$$

Here N is the total number of soil layers, r_i (unitless) is the root fraction within soil layer i , ψ_{\max} (mm) is the maximum value of soil matrix potential before leaves wilt (-1.5×10^5 mm), $\psi_{\text{sat},i}$ (mm) is the saturated soil water matrix potential, and ψ_i (mm) is the soil water matrix potential. The factor $(\psi_{\max} - \psi_i) / (\psi_{\max} + \psi_{\text{sat},i})$ ranges from 0 at the permanent wilting point to 1 at field capacity [Dai et al., 2004].

The maximum rate of carboxylation allowed by the capacity to generate RuBP (i.e., the light-limited rate), w_j ($\text{mol m}^{-2} \text{s}^{-1}$) is

$$w_j = \begin{cases} \frac{J(c_i - \Gamma_*)}{c_i + 2\Gamma_*} & \text{for } C_3 \text{ plants} \\ J & \text{for } C_4 \text{ plants} \end{cases} \quad (A6)$$

Here J is the electron transport rate for given absorbed PAR, and it is defined as

$$J = \min\left(\epsilon I_s, \frac{J_m}{4}\right) \quad (A7)$$

where I_s refers to the PAR absorbed by the leaf ($\text{mol m}^{-2} \text{s}^{-1}$) and ϵ is the quantum yield of electron transport. J_m is potential electron transport rate ($\text{mol m}^{-2} \text{s}^{-1}$), which varies with leaf temperature and soil water [Tezara et al., 1999]:

$$J_m = J_{\max} f_T(T_l) f_w(\theta) \quad (A8)$$

with J_{\max} being the potential maximum (light saturated) electron transport rate ($J_{\max} = 2.1V_{\max}$) and $f_T(T_I)$ the temperature dependence of J_m :

$$f_T(T_I) = \frac{e^{\left(\frac{10 \times 0.10 \times E_a}{298 \times R \times T_I}\right)} \times \left(1 + e^{\left(\frac{298 \times S - H}{298 \times R}\right)}\right)}{1 + e^{\left(\frac{S \times T_I - H}{R \times T_I}\right)}} \quad (\text{A9})$$

Here H is a curvature parameter for J_{\max} ($H = 2.2 \times 10^5 \text{ J mol}^{-1} \text{ K}^{-1}$), R is the universal gas constant ($R = 8.314 \text{ J mol}^{-1} \text{ K}^{-1}$), S is the electron-transport temperature response parameter ($S = 710 \text{ J mol}^{-1}$), and E_a is the activation energy ($E = 37,000 \text{ J mol}^{-1}$).

Finally, the carbon compound export limitation (C_3 plants) or PEP-carboxylase limitation (C_4 plants) is defined as follows:

$$w_e = \begin{cases} 0.5V_m & \text{for } C_3 \text{ plants} \\ 2 \times 10^4 V_m \frac{C_i}{P_{\text{atm}}} & \text{for } C_4 \text{ plants} \end{cases} \quad (\text{A10})$$

where P_{atm} is the atmospheric pressure at surface (Pa).

Considering the nitrogen limitation on potential GPP, it is calculated from leaf photosynthetic rate without nitrogen constraint. The nitrogen required to achieve this potential GPP is diagnosed, and the actual GPP is decreased for nitrogen limitation. Thus, potential GPP must be reduced by multiplying the photosynthetic parameter V_m (maximum rate of carboxylation) by a PFT-specific factor scaled between 0 and 1 that represents nitrogen constraints on GPP [Lawrence *et al.*, 2011]:

$$V_m = V_{\max} f_T(T_I) f_w(\theta) f(N) \quad (\text{A11})$$

where $f(N)$ are the PFT-dependent nitrogen factors.

A2. JULES

As CLM4CN, the leaf photosynthesis is estimated as the minimum of three assimilation limited rates: the Rubisco-limited rate w_c , the light-limited rate w_j , and the carbon compound export limitation (C_3 plants) or PEP-carboxylase limitation (C_4 plants) w_e . Further details on the photosynthesis parameterization and the differences with respect to CLM4CN are given by Clark *et al.* [2011].

A3. ORCHIDEE

C_3 and C_4 photosynthesis is calculated following Farquhar *et al.* [1980] and Collatz *et al.* [1992], respectively. Considering the C_3 PFTs, the leaf assimilation (A) is defined as follows [Krinner *et al.*, 2005]:

$$A = V_c \left(1 - \frac{\Gamma^*}{C_i}\right) \quad (\text{A12})$$

where V_c ($\mu\text{mol m}^{-2} \text{ s}^{-1}$) is the rate of carboxylation, Γ^* (ppm) is the CO_2 compensation point when there is no nonphotorespiratory respiration, and C_i is the CO_2 concentration at the carboxylation site.

The rate of carboxylation is expressed as the more limiting factor between the Rubisco activity W_c and RuBP regeneration W_j ($\mu\text{mol m}^{-2} \text{ s}^{-1}$):

$$V_c = \min(W_c, W_j) \quad (\text{A13})$$

The Rubisco-limited rate is given by

$$W_c = \frac{V_{c\max} + C_i}{C_i + K_c \left(1 + \frac{O_i}{K_o}\right)} \quad (\text{A14})$$

with $V_{c\max}$ ($\mu\text{mol m}^{-2} \text{ s}^{-1}$) representing the maximum rate of RuBP carboxylation, K_c and K_o are the Michaelis-Menten constants for enzyme catalytic activity for CO_2 and O_2 , respectively, and O_i is the intercellular concentration of oxygen.

The RuBP regeneration-limited rate is defined as follows:

$$W_j = \frac{V_j}{1 + \frac{2I_j}{C_i}} \quad (\text{A15})$$

where V_j is the potential rate of RuBP regeneration and it depends on the incident photon flux I . V_j can be empirically described using a nonrectangular hyperbola,

$$V_j = \frac{1}{2\Theta} \left[\alpha_j I + V_{j\max} - \sqrt{(\alpha_j I + V_{j\max})^2 - 4\Theta\alpha_j I V_{j\max}} \right] \quad (\text{A16})$$

where α_j is the quantum yield of RuBP regeneration, $V_{j\max}$ is the maximum potential rate of RuBP regeneration at quantum saturation, and Θ is the curvature of the quantum response.

The water stress influences the photosynthetic capacity (i.e., $V_{j\max}$ and $V_{c\max}$). The water stress factor γ_w is defined after *McMurtrie et al.* [1990]:

$$\gamma_w = \begin{cases} 1 & \text{if } f_w > f_{w1} \\ 1 - \frac{f_w - f_{w0}}{f_{w1} - f_{w0}} & \text{if } f_{w0} < f_w < f_{w1} \\ 0 & \text{if } f_w < f_{w0} \end{cases} \quad (\text{A17})$$

where f_w is the water fraction available for the plant in the root zone ($f_w = 0$ at wilting point and $f_w = 1$ at field capacity); $f_{w0} = 0.028$ and $f_{w1} = 0.5$ are the soil water fractions inducing, respectively, closure and maximum opening of the stomata [*Krinner et al.*, 2005].

In addition, the maximum rubisco-limited potential photosynthetic capacity (that is unstressed photosynthetic capacity at optimum temperature) is parameterized as a function of leaf age, increasing from a relatively low initial value to a prescribed optimum during the first days after leaf onset, staying constant at this maximum for a given period (a few months, depending on the PFT), and then decreasing to a lower value for old leaves [*Ishida et al.*, 1999]. Thus, the photosynthetic capacity (given through $V_{j\max}$ and $V_{c\max}$, respectively) depends on leaf age through:

$$V_{(c,j)\max}(a) = V_{(c,j)\max,\text{opt}} \times e_{\text{rel}}(a) \quad (\text{A18})$$

where a is the leaf age, e_{rel} is the relative photosynthetic efficiency, and $V_{(c,j)\max,\text{opt}}$ is the PFT-dependent optimum photosynthetic capacity. Four cohorts of increasing leaf age are defined between onset and leaf fall from senescence.

Glossary

APAR	absorbed photosynthetically active radiation
CESM1-BGC	Community Earth System Model, version 1–BioGeoChemistry
CLMCN4	Community Land Model Carbon-Nitrogen version 4
CMIP5	Fifth Climate Model Intercomparison Project
COS	carbonyl sulfide
CRU	Climate Research Unit
DGVM	Dynamic Global Vegetation Models
DOE	U.S. Department of Energy
ESM	Earth System Model
fAPAR	Fraction of Absorbed Photosynthetically Active Radiation
FLUXNET	FLUX NETWORK
GOSAT	Greenhouse Gases Observing Satellite
GPP	gross primary production
HadGEM2-ES	Hadley Centre Global Environmental Model version 2 Earth System
IAV	interannual variability
ICOS	Integrated Carbon Observation System
IPSL-CM5A-MR	Institut Pierre Simon Laplace Coupled Model version 5A–Medium Resolution
ITCZ	Intertropical Convergence Zone
JJA	June July August
JULES	Joint UK Land Environment Simulator

LAI	leaf area index
LMDz	Laboratoire de Météorologie Dynamique
LUE	light use efficiency
MODIS	Moderate Resolution Imaging Spectroradiometer
MPI-ESM	Max Planck Institute Earth System Model
MTE	model tree ensemble
NCEP	National Centers for Environmental Prediction
NEE	net ecosystem exchange
NEON	National Ecological Observatory Network
NorESM1-ME	Norwegian Earth System Model
NPP	net primary production
ORCHIDEE	ORganizing Carbon and Hydrology in Dynamic Ecosystems
PAR	photosynthetically active radiation
PFT	plant functional type
RCP	Representative Concentration Pathways
R_{eco}	ecosystem respiration
RMSD	root-mean-square deviation
SIF	Sun-induced fluorescence

Acknowledgments

We acknowledge the World Climate Research Programme's Working Group on Coupled Modeling, which is responsible for CMIP, and we thank the climate modeling groups (listed in Table 1 of this paper) for producing and making available their model output. For CMIP the U.S. Department of Energy's Program for Climate Model Diagnosis and Intercomparison provides coordinating support and led development of software infrastructure in partnership with the Global Organization for Earth System Science Portals. We thank also the principal investigators of the eddy covariance sites responsible for the measurements and the whole FLUXNET community. Data used in this work can be downloaded from the European database at www.europe-fluxdata.eu. We also thank M. Reichstein and M. Jung for providing MTE-GPP data through the site: <https://www.bgc-jena.mpg.de/bgi/index.php/Services/Overview>, as well as the Eumetsat for the GOME-2 data (<http://avdc.gsfc.nasa.gov>). CMIP5 data can be freely downloaded from the following link: <http://pcmdi9.llnl.gov/esgf-web-fe/>, while information on how to retrieve TRENDY outputs are given in <http://dgv.m.ceh.ac.uk/node/9>. MODIS GPP data can be downloaded from the following link: <http://ntsg.umt.edu/>. Finally, outputs from CARBONES are at <http://www.carbones.eu/wcmqs/>. This work was supported by the European Commission's Seventh Framework Programme under grant agreement 238366 (GREENCYCLESII) and 282672 (EMBRACE), while Jones was supported by the Joint DECC/Defra Met Office Hadley Centre Climate Program (GA01101). We also wish to thank Gregory Okin and two anonymous reviewers for their positive comments on this manuscript.

The Editor for this paper was Gregory Okin. He thanks Steven Running and one anonymous reviewer for their review assistance on this manuscript.

References

- Acosta, M., M. Pavelka, L. Montagnani, W. Kutsch, A. Lindroth, R. Juszczak, and D. Janouš (2013), Soil surface CO₂ efflux measurements in Norway spruce forests: Comparison between four different sites across Europe—From boreal to alpine forest, *Geoderma*, *192*, 295–303.
- Agreen, G. I., R. E. McMurtrie, W. J. Parton, J. Pastor, and H. H. Shugart (1991), State-of-the-art models of production-decomposition linkages in conifer and grassland ecosystems, *Ecol. Appl.*, *1*, 118–138.
- Anav, A., L. Menut, D. Khvorostyanov, and N. Viovy (2011), Impact of tropospheric ozone on the Euro-Mediterranean vegetation, *Global Change Biol.*, *17*, 2342–2359.
- Anav, A., P. Friedlingstein, M. Kidston, L. Bopp, P. Ciais, P. M. Cox, C. D. Jones, M. Jung, R. B. Myneni, and Z. Zhu (2013), Evaluating the land and ocean components of the global carbon cycle in the CMIP5 Earth System Models, *J. Clim.*, *26*, 6801–6843.
- Arora, V. K., et al. (2013), Carbon-concentration and carbon-climate feedbacks in CMIP5 Earth system models, *J. Clim.*, *26*, 5289–5314.
- Asaf, D., E. Rotenberg, F. Tatarinov, U. Dicken, S. A. Montzka, and D. Yakir (2013), Ecosystem photosynthesis inferred from measurements of carbonyl sulphide flux, *Nat. Geosci.*, *6*, 1–5.
- Aubinet, M., B. Chermanne, M. Vandenhoute, B. Longdoz, M. Yernaux, and F. Laitat (2001), Long term carbon dioxide exchange above a mixed forest in the Belgian Ardennes, *Agric. For. Meteorol.*, *108*, 293–315.
- Aubinet, M., T. Vesala, and D. Papale (Eds) (2012), *Eddy Covariance—A Practical Guide to Measurement and Data Analysis*, Springer, Dordrecht, Netherlands.
- Baldocchi, D. (2003), Assessing the eddy covariance technique for evaluating carbon dioxide exchange rates of ecosystems: Past, present and future, *Global Change Biol.*, *9*, 479–492.
- Baldocchi, D., et al. (2001), FLUXNET: A new tool to study the temporal and spatial variability of ecosystem scale carbon dioxide, water vapor, and energy flux densities, *Bull. Am. Meteorol. Soc.*, *82*, 2415–2434.
- Barman, R., A. K. Jain, and M. Liang (2014), Climate-driven uncertainties in modeling terrestrial gross primary production: A site level to global-scale analysis, *Global Change Biol.*, *20*, 1394–1411.
- Battin, T. J., L. A. Kaplan, S. Findlay, C. S. Hopkins, E. Marti, A. I. Packman, J. D. Newbold, and F. Sabater (2009), The boundless carbon cycle, *Nat. Geosci.*, *2*, 598–600.
- Beer, C., et al. (2009), Temporal and among-site variability of inherent water use efficiency at the ecosystem level, *Global Biogeochem. Cycles*, *23*, GB2018, doi:10.1029/2008GB003233.
- Beer, C., et al. (2010), Terrestrial gross carbon dioxide uptake: Global distribution and covariation with climate, *Science*, *329*, 834–838.
- Bentsen, M., et al. (2013), The Norwegian Earth System Model, NorESM1-M—Part 1: Description and basic evaluation of the physical climate, *Geosci. Model Dev.*, *6*, 687–720.
- Berbigier, P., J. M. Bonnefond, and P. Mellmann (2001), CO₂ and water vapour fluxes for 2 years above Euroflux forest site, *Agric. For. Meteorol.*, *108*, 183–197.
- Best, M. J., et al. (2011), The Joint UK Land Environment Simulator (JULES), model description—Part 1: Energy and water fluxes, *Geosci. Model Dev.*, *4*, 677–699.
- Betts, A. K. (2004), Understanding hydrometeorology using global models, *Bull. Am. Meteorol. Soc.*, *85*, 1673–1688.
- Blonquist, J. M., Jr., S. A. Montzka, J. W. Munger, D. Yakir, A. R. Desai, D. Dragoni, T. J. Griffis, R. K. Monson, R. L. Scott, and D. R. Bowling (2011), The potential of carbonyl sulfide as a proxy for gross primary production at flux tower sites, *J. Geophys. Res.*, *116*, G04019, doi:10.1029/2011JG001723.
- Braswell, B. H., W. J. Sacks, E. Linder, and D. S. Schimel (2005), Estimating diurnal to annual ecosystem parameters by synthesis of a carbon flux model with eddy covariance net ecosystem exchange observations, *Global Change Biol.*, *11*, 335–355.
- Canadell, J. G., et al. (2000), Carbon metabolism of the terrestrial biosphere: A multitechnique approach for improved understanding, *Ecosystems*, *3*, 115–130.
- Carvalho, N., et al. (2008), Implications of the carbon cycle steady state assumptions for biogeochemical modeling performance and inverse parameter retrieval, *Global Biogeochem. Cycles*, *22*, GB2007, doi:10.1029/2007GB003033.
- Chapin, F. S., P. A. Matson, and H. A. Mooney (2002), *Principles of Terrestrial Ecosystem Ecology*, Springer, New York.

- Chen, J. M., G. Mo, J. Pisek, F. Deng, M. Ishozawa, and D. Chan (2012), Effects of foliage clumping on global terrestrial gross primary productivity, *Global Biogeochem. Cycles*, *26*, GB1019, doi:10.1029/2010GB003996.
- Churakova, O. V. (Sidorova), W. Eugster, S. Etzold, P. Cherubini, S. Zielis, M. Saurer, R. Siegwolf, and N. Buchmann (2014), Increasing relevance of spring temperatures for Norway spruce trees in Davos, Switzerland, after the 1950s, *Trees*, *28*, 183–191.
- Churkina, G., and S. Running (1998), Contrasting climatic controls on the estimated productivity of global terrestrial biomes, *Ecosystems*, *1*, 206–215.
- Ciais, P., et al. (1997), A three-dimensional synthesis study of $\delta^{18}\text{O}$ in atmospheric CO_2 : 1. Surface fluxes, *J. Geophys. Res.*, *102*(D5), 5857–5872, doi:10.1029/96JD02360.
- Ciais, P., et al. (2005), Europe-wide reduction in primary productivity caused by the heat and drought in 2003, *Nature*, *437*, 529–533.
- Ciais, P., et al. (2013), Chapter 6: Carbon and other biogeochemical cycles, in *Climate Change 2013 The Physical Science Basis*, edited by T. Stocker, D. Qin, and G.-K. Plattner, Cambridge Univ. Press, Cambridge, U. K.
- Ciais, P., et al. (2014), Current systematic carbon-cycle observations and the need for implementing a policy-relevant carbon observing system, *Biogeosciences*, *11*, 3547–3602.
- Clark, D. A., S. C. Piper, C. D. Keeling, and D. B. Clark (2003), Tropical rain forest tree growth and atmospheric carbon dynamics linked to interannual temperature variation during 1984–2000, *Proc. Natl. Acad. Sci. U.S.A.*, *100*, 5852–5857.
- Clark, D. B., et al. (2011), The Joint UK Land Environment Simulator (JULES), model description—Part 2: Carbon fluxes and vegetation dynamics, *Geosci. Model Dev.*, *4*, 701–722.
- Collatz, G. J., J. T. Ball, C. Grivet, and J. A. Berry (1991), Physiological and environmental regulation of stomatal conductance, photosynthesis, and transpiration: A model that includes a laminar boundary layer, *Agric. For. Meteorol.*, *54*, 107–136.
- Collatz, G. J., M. Ribas-Carbo, and J. A. Berry (1992), Coupled photosynthesis-stomatal conductance model for leaves of C_4 plants, *Aust. J. Plant Physiol.*, *19*, 519–538.
- Collins, W. J., et al. (2011), Development and evaluation of an Earth-System model—HadGEM2, *Geosci. Model Dev.*, *4*, 1051–1075.
- Cox, P., and C. Jones (2008), Illuminating the modern dance of climate and CO_2 , *Science*, *321*, 1642–1644.
- Cox, P. M., R. A. Betts, C. B. Bunton, R. L. H. Essery, P. R. Rowntree, and J. Smith (1999), The impact of new land surface physics on the GCM simulation of climate and climate sensitivity, *Clim. Dyn.*, *15*, 183–203.
- Cramer, W., D. W. Kicklighter, A. Bondeau, B. Moore III, G. Churkina, B. Nemry, A. Ruimy, A. L. Schloss, and ThE. Participants OF. ThE. Potsdam NpP. Model Intercomparison (1999), Comparing global models of terrestrial net primary productivity (NPP): Overview and key results, *Global Change Biol.*, *5*, 1–15.
- Cramer, W., et al. (2001), Global response of terrestrial ecosystem structure and function to CO_2 and climate change: Results from six dynamic global vegetation models, *Global Change Biol.*, *7*, 357–373.
- Dai, Y., R. E. Dickinson, and Y.-P. Wang (2004), A two big leaf model for canopy temperature, photosynthesis, and stomatal conductance, *J. Clim.*, *17*, 2281–2299.
- Dalmonech, D., S. Zaehle, G. J. Schürmann, V. Brovkin, C. Reick, and R. Schnur (2015), Separation of the effects of land and climate model errors on simulated contemporary land carbon cycle trends in the MPI Earth system model version 1, *J. Clim.*, *28*, 272–291.
- Damm, A., et al. (2010), Remote sensing of sun-induced fluorescence to improve modeling of diurnal courses of gross primary production (GPP), *Global Change Biol.*, *16*, 171–186.
- Dargaville, R. J., et al. (2002), Evaluation of terrestrial carbon cycle models with atmospheric CO_2 measurements: Results from transient simulations considering increasing CO_2 , climate, and land-use effects, *Global Biogeochem. Cycles*, *16*(4), 1092, doi:10.1029/2001GB001426.
- Denman, K., et al. (2007), Couplings between changes and biogeochemistry, in *Climate Change 2007: The Physical Science Basis. Contribution of Working Group Report of the Intergovernmental Panel on Climate Change*, edited by S. Solomon et al., pp. 499–588, Cambridge Univ. Press, Cambridge, U. K.
- Dolman, A. J., E. J. Moors, and J. A. Elbers (2002), The carbon uptake of a mid latitude pine forest growing on sandy soil, *Agric. For. Meteorol.*, *111*, 157–170.
- Dufresne, J.-L., et al. (2013), Climate change projections using the IPSL-CM5 Earth system model: From CMIP3 to CMIP5, *Clim. Dyn.*, *40*, 2123–2165.
- Dunne, J. P., et al. (2012), GFDL's ESM2 global coupled climate-carbon Earth System Models. Part I: Physical formulation and baseline simulation characteristics, *J. Clim.*, *25*, 6646–6665.
- Farquhar, G. D., S. von Caemmerer, and J. A. Berry (1980), A biochemical model of photosynthetic CO_2 assimilation in leaves of C_3 species, *Planta*, *149*, 78–90.
- Farquhar, G. D., J. Lloyd, J. A. Taylor, L. B. Flanagan, J. P. Syvertsen, K. T. Hubick, S. C. Wong, and J. R. Ehleringer (1993), Vegetation effects on the isotope composition of oxygen in atmospheric CO_2 , *Nature*, *363*, 439–443.
- Frankenberg, C., et al. (2011), New global observations of the terrestrial carbon cycle from GOSAT: Patterns of plant fluorescence with gross primary productivity, *Geophys. Res. Lett.*, *38*, L17706, doi:10.1029/2011GL048738.
- Friedlingstein, P., et al. (2006), Climate-carbon cycle feedback analysis: Results from the C^4MIP model intercomparison, *J. Clim.*, *19*, 3373–3353.
- Friend, A. D., et al. (2007), FLUXNET and modelling the global carbon cycle, *Global Change Biol.*, *13*(3), 610–633, doi:10.1111/j.1365-2486.2006.01223.x.
- Gent, P. R., et al. (2011), The Community Climate System Model version 4, *J. Clim.*, *24*, 4973–4991.
- Gervois, S., P. Ciais, N. de Noblet-Ducoudre, N. Brisson, N. Vuichard, and N. Viovy (2008), Carbon and water balance of European croplands throughout the 20th century, *Global Biogeochem. Cycles*, *22*, GB2022, doi:10.1029/2007GB003018.
- Gobron, N., A. Belward, B. Pinty, and W. Knorr (2010), Monitoring biosphere vegetation 1998–2009, *Geophys. Res. Lett.*, *37*, L15402, doi:10.1029/2010GL043870.
- Goetz, S. J., and S. D. Prince (1999), Modelling terrestrial carbon exchange and storage: evidence and implications of functional convergence in light-use efficiency, *Advances in Ecological Research*, *28*, 57–92.
- Goll, D. S., et al. (2012), Nutrient limitation reduces land carbon uptake in simulations with a model of combined carbon, nitrogen and phosphorus cycling, *Biogeosciences*, *9*, 3547–3569.
- Granier, A., et al. (2007), Evidence for soil water control on carbon and water dynamics in European forests during the extremely dry year: 2003, *Agric. For. Meteorol.*, *143*, 123–145.
- Granire, A., et al. (2000), The carbon balance of a young Beech forest, *Funct. Ecol.*, *14*, 312–325.
- Grünwald, T., and C. Bernhofer (2007), A decade of carbon, water and energy flux measurements of an old spruce forest at the anchor station Tharandt, *Tellus, Ser. B*, *59*, 387–396.
- Guanter, L., et al. (2012), Retrieval and global assessment of terrestrial chlorophyll fluorescence from GOSAT space measurements, *Remote Sens. Environ.*, *121*, 236–251.

- Guanter, L., et al. (2014), Global and time-resolved monitoring of crop photosynthesis with chlorophyll fluorescence, *Proc. Natl. Acad. Sci. U.S.A.*, *111*, E1,327–E1,333.
- Hajima, T., K. Tachiiri, A. Ito, and M. Kawamiya (2014), Uncertainty of concentration-terrestrial carbon feedback in Earth system models, *J. Clim.*, *27*, 3425–3445.
- Heinsch, F. A., et al. (2006), Evaluation of remote sensing based terrestrial productivity from MODIS using regional tower eddy flux network observations, *IEEE Trans. Geosci. Remote Sens.*, *44*(7), 1908–1925.
- Hilker, T., N. C. Coops, M. A. Wulder, A. T. Black, and R. D. Guy (2008), The use of remote sensing in light use efficiency based models of gross primary production: A review of current status and future requirements, *Sci. Total Environ.*, *404*, 411–423.
- Hollinger, D. Y., S. M. Goltz, E. A. Davidson, J. T. Lee, K. Tu, and H. T. Valentine (1999), Seasonal patterns and environmental control of carbon dioxide and water vapour exchange in an ecotonal boreal forest, *Global Change Biol.*, *5*, 891–902.
- Hourdin, F., et al. (2006), The LMDZ4 general circulation model: Climate performance and sensitivity to parametrized physics with emphasis on tropical convection, *Clim. Dyn.*, *27*, 787–813.
- Ishida, A., A. Uemura, N. Koike, Y. Matsumoto, and A. Lai Hoe (1999), Interactive effects of leaf age and self-shading on leaf structure, photosynthetic capacity and chlorophyll fluorescence in the rain forest tree, *dryobalanops aromatica*, *Tree Physiol.*, *19*, 741–747.
- Jaeger, E. B., R. Stöckli, and S. I. Seneviratne (2009), Analysis of planetary boundary layer fluxes and land-atmosphere coupling in the regional climate model CLM, *J. Geophys. Res.*, *114*, D17106, doi:10.1029/2008JD011658.
- Janssens, I. A., et al. (2003), Europe's terrestrial biosphere absorbs 7 to 12% of European anthropogenic CO₂ emissions, *Science*, *300*, 1538–1542.
- Ji, D., et al. (2014), Description and basic evaluation of BNU-ESM version 1, *Geosci. Model Dev. Discuss.*, *7*, 1601–1647.
- Johns, T. C., et al. (2006), The new Hadley Centre climate model HadGEM1: Evaluation of coupled simulations, *J. Clim.*, *19*, 1327–1353.
- Joiner, J., Y. Yoshida, A. P. Vasilkov, Y. Yoshida, L. A. Corp, and E. M. Middleton (2011), First observations of global and seasonal terrestrial chlorophyll fluorescence from space, *Biogeosciences*, *8*, 637–651.
- Joiner, J., L. Guanter, R. Lindstrot, M. Voigt, A. P. Vasilkov, E. M. Middleton, K. F. Huemmrich, Y. Yoshida, and C. Frankenberg (2013), Global monitoring of terrestrial chlorophyll fluorescence from moderate-spectral-resolution near-infrared satellite measurements: Methodology, simulations, and application to GOME-2, *Atmos. Meas. Tech.*, *6*, 2803–2823.
- Jung, M., et al. (2007), Uncertainties of modeling gross primary productivity over Europe: A systematic study on the effects of using different drivers and terrestrial biosphere models, *Global Biogeochem. Cycles*, *21*, GB4021, doi:10.1029/2006GB002915.
- Jung, M., M. Verstraete, N. Gobron, M. Reichstein, D. Papale, A. Bondeau, M. Robustelli, and B. Pinty (2008), Diagnostic assessment of European gross primary production, *Global Change Biol.*, *14*, 2349–2364, doi:10.1111/j.1365-2486.2008.01647.x.
- Jung, M., M. Reichstein, and A. Bondeau (2009), Towards global empirical upscaling of FLUXNET eddy covariance observations: Validation of a model tree ensemble approach using a biosphere model, *Biogeosciences*, *6*, 2001–2013.
- Jung, M., et al. (2010), Recent decline in the global land evapotranspiration trend due to limited moisture supply, *Nature*, *467*, 951–954.
- Jung, M., et al. (2011), Global patterns of land-atmosphere fluxes of carbon dioxide, latent heat, and sensible heat derived from eddy covariance, satellite, and meteorological observations, *J. Geophys. Res.*, *116*, G00J07, doi:10.1029/2010JG001566.
- Kicklighter, D. W., et al. (1999), A first-order analysis of the potential role of CO₂ fertilization to affect the global carbon budget: A comparison of four terrestrial biosphere models, *Tellus B*, *51*(2), 343–366.
- Knohl, A., E. D. Schulze, O. Kolle, and N. Buchmann (2003), Large carbon uptake by an unmanaged 250-year-old deciduous forest in Central Germany, *Agric. For. Meteorol.*, *118*, 151–167.
- Koffi, E. N., P. J. Rayner, M. Scholze, and C. Beer (2012), Atmospheric constraints on gross primary productivity and net ecosystem productivity: Results from a carbon-cycle data assimilation system, *Global Biogeochem. Cycles*, *26*, GB1024, doi:10.1029/2010GB003900.
- Krinner, G., N. Viovy, N. de Noblet-Ducoudré, J. Ogée, J. Polcher, P. Friedlingstein, P. Ciais, S. Sitch, and I. C. Prentice (2005), A dynamic global vegetation model for studies of the coupled atmosphere-biosphere system, *Global Biogeochem. Cycles*, *19*, GB1015, doi:10.1029/2003GB002199.
- Kuppel, S., F. Chevallier, and P. Peylin (2013), Quantifying the model structural error in carbon cycle data assimilation systems, *Geosci. Model Dev.*, *6*, 45–55.
- Lasslop, G., M. Reichstein, D. Papale, A. D. Richardson, A. Arneeth, A. Barr, P. Stoy, and G. Wohlfahrt (2010), Separation of net ecosystem exchange into assimilation and respiration using a light response curve approach: Critical issues and global evaluation, *Global Change Biol.*, *16*, 187–208, doi:10.1111/j.1365-2486.2009.02041.x.
- Lawrence, D., et al. (2011), Parameterization improvements and functional and structural advances in version 4 of the Community Land Model, *J. Adv. Model. Earth Syst.*, *3*, M03001, doi:10.1029/2011MS000045.
- Le Quéré, C., et al. (2009), Trends in the sources and sinks of carbon dioxide, *Nat. Geosci.*, *2*, 831–836.
- Lin, J. C., M. R. Pejam, E. Chan, S. C. Wofsy, E. W. Gottlieb, H. A. Margolis, and J. H. McCaughey (2011), Attributing uncertainties in simulated biospheric carbon fluxes to different error sources, *Global Biogeochem. Cycles*, *25*, GB2018, doi:10.1029/2010GB003884.
- Lin, J. L. (2007), Interdecadal variability of ENSO in 21 IPCC AR4 coupled GCMs, *Geophys. Res. Lett.*, *34*, L12702, doi:10.1029/2006GL028937.
- Long, S. P., and C. J. Bernacchi (2003), Gas exchange measurements, what can they tell us about the underlying limitation to photosynthesis? Procedures and sources of error, *J. Exp. Bot.*, *54*, 2393–2401.
- Ma, J., X. Yan, W. Dong, and J. Chou (2015), Gross primary production of global forest ecosystems has been overestimated, *Nat. Sci. Rep.*, *5*, 10820, doi:10.1038/srep10820.
- Magnani, F., et al. (2007), The human footprint in the carbon cycle of temperate and boreal forests, *Nature*, *447*, 848–850.
- Mahecha, M. D., et al. (2010), Comparing observations and process-based simulations of biosphere-atmosphere exchanges on multiple timescales, *J. Geophys. Res.*, *115*, G02003, doi:10.1029/2009JG001016.
- McGuire, A. D., L. A. Joyce, D. W. Kicklighter, J. M. Melillo, G. Esser, and C. J. Vorosmarty (1993), Productivity response of climax temperate forests to elevated temperature and carbon dioxide: A North American comparison between two global models, *Clim. Change*, *24*, 287–310.
- McGuire, A. D., et al. (2001), Carbon balance of the terrestrial biosphere in the twentieth century: analyses of CO₂ climate and land use effects with four process-based ecosystem models, *Global Biogeochem. Cycles*, *15*(1), 183–206, doi:10.1029/2000GB001298.
- McMurtrie, R., D. Rook, and F. Kelliher (1990), Modelling the yield of pinus radiata on a site limited by water and nitrogen, *For. Ecol. Manage.*, *30*, 381–413.
- Montagnani, L., et al. (2009), A new mass conservation approach to the study of CO₂ advection in an alpine forest, *J. Geophys. Res. Atm.*, *114*, D07306, doi:10.1029/2008JD010650.
- Monteith, J. L. (1972), Solar radiation and production in tropical ecosystems, *J. Appl. Ecol.*, *9*, 747–766.
- Monteith, J. L. (1977), Climate and efficiency of crop production in Britain, *Philos. Trans. R. Soc., B*, *281*, 277–294.
- Moorcroft, P. R. (2006), How close are we to a predictive science of the biosphere?, *Trends Ecol. Evol.*, *21*, 400–407.

- Morales, P., et al. (2005), Comparing and evaluating process-based ecosystem model predictions of carbon and water fluxes in major European forest biomes, *Global Change Biol.*, *11*, 2211–2233, doi:10.1111/j.1365-2486.2005.01036.x.
- Murray-Tortarolo, G., et al. (2013), Evaluation of land surface models in reproducing satellite-derived LAI over the high-latitude Northern Hemisphere. Part I: Uncoupled DGVMs, *Remote Sens.*, *5*, 4819–4838.
- Myneni, R., S. Hoffman, J. Glassy, Y. Zhang, P. Votava, R. Nemani, S. Running, and J. Privette (2002), Global products of vegetation leaf area and fraction absorbed PAR from year one of MODIS data, *Remote Sens. Environ.*, *83*, 214–231.
- Nemani, R., C. Keeling, H. Hashimoto, W. Jolly, S. Piper, C. Tucker, R. Myneni, and S. Running (2003), Climate-driven increases in global terrestrial net primary production from 1982 to 1999, *Science*, *300*, 1560–1563.
- Oleson, K. W., et al. (2010), Technical description of version 4.0 of the Community Land Model (CLM), *NCAR Tech. Note NCAR/TN-478+STR*, doi:10.5065/D6FB50WZ.
- Parazoo, N. C., et al. (2014), Terrestrial gross primary production inferred from satellite fluorescence and vegetation models, *Global Change Biol.*, *20*, 3103–3121.
- Piao, S., P. Friedlingstein, P. Ciais, N. Viovy, and J. Demarty (2007), Growing season extension and its impact on terrestrial carbon cycle in the Northern Hemisphere over the past 2 decades, *Global Biogeochem. Cycles*, *21*, GB3018, doi:10.1029/2006GB002888.
- Piao, S., P. Ciais, P. Friedlingstein, N. de Noblet-Ducoudré, P. Cadule, N. Viovy, and T. Wang (2009), Spatiotemporal patterns of terrestrial carbon cycle during the 20th century, *Global Biogeochem. Cycles*, *23*, GB4026, doi:10.1029/2008GB003339.
- Piao, S., et al. (2013), Evaluation of terrestrial carbon cycle models for their response to climate variability and to CO₂ trends, *Global Change Biol.*, *19*, 2117–2132.
- Piao, S., et al. (2014), Evidence for a weakening relationship between interannual temperature variability and northern vegetation activity, *Nat. Commun.*, *5*, doi:10.1038/ncomms6018.
- Pilegaard, K., P. Hummelshøj, N. O. Jensen, and Z. Chen (2001), Two years of continuous CO₂ eddy-flux measurements over a Danish beech forest, *Agric. For. Meteorol.*, *107*, 29–41.
- Poulter, B., D. C. Frank, E. L. Hodson, and N. E. Zimmermann (2011), Impacts of land cover and climate data selection on understanding terrestrial carbon dynamics and the CO₂ airborne fraction, *Biogeosciences*, *8*, 2027–2036.
- Prentice, I. C., X. Liang, B. E. Medlyn, and Y.-P. Wang (2014), Reliable, robust and realistic: The three R's of next-generation land surface modelling, *Atmos. Chem. Phys. Discuss.*, *14*, 24,811–24,861.
- Rambal, S., R. Joffre, J. M. Ourcival, J. Cavender-Bares, and A. Rocheteau (2004), The growth respiration component in eddy CO₂ flux from a *Quercus ilex* Mediterranean forest, *Global Change Biol.*, *10*, 1460–1469.
- Randerson, J. T., et al. (2009), Systematic assessment of terrestrial biogeochemistry in coupled climate-carbon models, *Global Change Biol.*, *15*, 2462–2484, doi:10.1111/j.1365-2486.2009.01912.x.
- Rayner, P. J., M. Scholze, W. Knorr, T. Kaminski, R. Giering, and H. Widmann (2005), Two decades of terrestrial carbon fluxes from a carbon cycle data assimilation system (CCDAS), *Global Biogeochem. Cycles*, *19*, GB2026, doi:10.1029/2004GB002254.
- Reichstein, M., et al. (2005), On the separation of net ecosystem exchange into assimilation and ecosystem respiration: Review and improved algorithm, *Global Change Biol.*, *11*, 1424–1439, doi:10.1111/j.1365-2486.2005.001002.x.
- Reichstein, M., et al. (2007), Determinants of terrestrial ecosystem carbon balance inferred from European eddy covariance flux sites, *Geophys. Res. Lett.*, *34*, L01402, doi:10.1029/2006GL027880.
- Reichstein, M., P. C. Stoy, A. R. Desai, G. Lasslop, and A. D. Richardson (2012), Partitioning of net fluxes, in *Eddy Covariance: A Practical Guide to Measurement and Data Analysis*, edited by M. Aubinet, T. Vesala, and D. Papale, pp. 263–289, Springer, Netherlands.
- Richardson, A. D., et al. (2006), Comparing simple respiration models for eddy flux and dynamic chamber data, *Agric. For. Meteorol.*, *141*, 219–234.
- Running, S. W., R. R. Nemani, F. A. Heinsch, M. Zhao, M. Reeves, and H. Hashimoto (2004), A continuous satellite-derived measure of global terrestrial primary productivity: Future science and applications, *BioScience*, *56*(6), 547–560.
- Runyan, C. W., P. D'Odorico, and D. Lawrence (2012), Physical and biological feedbacks of deforestation, *Rev. Geophys.*, *50*, RG4006, doi:10.1029/2012RG000394.
- Ryan, M. G. (1991), A simple method for estimating gross carbon budgets for vegetation in forest ecosystems, *Tree Physiol.*, *9*, 255–266.
- Ryu, Y., et al. (2011), Integration of MODIS land and atmosphere products with a coupled-process model to estimate gross primary productivity and evapotranspiration from 1 km to global scales, *Global Biogeochem. Cycles*, *25*, GB4017, doi:10.1029/2011GB004053.
- Sellers, P. J., J. A. Berry, G. J. Collatz, C. B. Field, and F. G. Hall (1992), Canopy reflectance, photosynthesis, and transpiration. III: A reanalysis using improved leaf models and a new canopy integration scheme, *Remote Sens. Environ.*, *42*, 187–216.
- Sitch, S., et al. (2003), Evaluation of ecosystem dynamics, plant geography and terrestrial carbon cycling in the LPJ dynamic vegetation model, *Global Change Biol.*, *9*, 161–185.
- Sitch, S., P. M. Cox, W. J. Collins, and C. Huntingford (2007), Indirect radiative forcing of climate change through ozone effects on the land-carbon sink, *Nature*, *448*, 791–794.
- Sitch, S., et al. (2008), Evaluation of the terrestrial carbon cycle future plant geography and climate-carbon cycle feedbacks using five Dynamic Global Vegetation Models (DGVMs), *Global Change Biol.*, *14*, 2015–2039, doi:10.1111/j.1365-2486.2008.01626.x.
- Sitch, S., et al. (2015), Recent trends and drivers of regional sources and sinks of carbon dioxide, *Biogeosciences*, *12*, 653–679.
- Sjöström, M., et al. (2013), Evaluation of MODIS gross primary productivity for Africa using eddy covariance data, *Remote Sens. Environ.*, *131*, 275–286.
- Still, C. J., J. A. Berry, G. J. Collatz, and R. S. DeFries (2003), Global distribution of C₃ and C₄ vegetation: Carbon cycle implications, *Global Biogeochem. Cycles*, *17*(1), 1006, doi:10.1029/2001GB001807.
- Suni, T., J. Rinne, A. Reissell, N. Altimir, P. Keronen, U. Rannik, M. D. Maso, M. Kulmala, and T. Vesala (2003a), Long-term measurements of surface fluxes above a Scots pine forest in Hyttiala, southern Finland, 1996–2001, *Boreal Environ. Res.*, *8*, 287–301.
- Suni, T., et al. (2003b), Air temperature triggers the commencement of evergreen boreal forest photosynthesis in spring, *Global Change Biol.*, *9*, 1410–1426.
- Taylor, K. E. (2001), Summarizing multiple aspects of model performance in a single diagram, *J. Geophys. Res.*, *106*, 7183–7192, doi:10.1029/2000JD900719.
- Taylor, K. E., R. J. Stouffer, and G. A. Meehl (2012), An overview of CMIP5 and the experiment design, *Bull. Am. Meteorol. Soc.*, *90*, 485–498, doi:10.1175/BAMS-D-11-00094.1.
- Tezara, W., V. J. Mitchell, S. D. Driscoll, and D. W. Lawlor (1999), Water stress inhibits plant photosynthesis by decreasing coupling factor and ATP, *Nature*, *401*, 914–917.
- Thornton, P. E., and N. A. Rosenbloom (2005), Ecosystem model spin-up: Estimating steady state conditions in a coupled terrestrial carbon and nitrogen cycle model, *Ecol. Modell.*, *189*, 25–48.

- Thornton, P. E., J.-F. Lamarque, N. A. Rosenbloom, and N. M. Mahowald (2007), Influence of carbon-nitrogen cycle coupling on land model response to CO₂ fertilization and climate variability, *Global Biogeochem. Cycles*, *21*, GB4018, doi:10.1029/2006GB002868.
- Thornton, P. E., et al. (2009), Carbon-nitrogen interactions regulate climate-carbon cycle feedbacks: Results from an atmosphere-ocean general circulation model, *Biogeosciences*, *6*, 2099–2120.
- Tjoelker, M. G., J. Oleksyn, and P. B. Reich (2001), Modelling respiration of vegetation: Evidence for a general temperature dependent Q₁₀, *Global Change Biol.*, *7*, 223–230.
- Todd-Brown, K. E. O., J. T. Randerson, W. M. Post, F. M. Hoffman, C. Tarnocai, E. A. G. Schuur, and S. D. Allison (2013), Causes of variation in soil carbon simulations from CMIP5 Earth system models and comparison with observations, *Biogeosciences*, *10*, 1717–1736.
- Traore, A. K., P. Ciais, N. Vuichard, B. Poulter, N. Viovy, M. Guimberteau, M. Jung, R. Myneni, and J. B. Fisher (2014), Evaluation of the ORCHIDEE ecosystem model over Africa against 25-years of satellite-based water and carbon measurements, *J. Geophys. Res. Biogeosci.*, *119*, 1554–1575, doi:10.1002/2014JG002638.
- Turner, D. P., et al. (2005), Site-level evaluation of satellite-based global terrestrial gross primary production and net primary production monitoring, *Global Change Biol.*, *11*, 666–684.
- Urbanski, S., et al. (2007), Factors controlling CO₂ exchange on timescales from hourly to decadal at Harvard forest, *J. Geophys. Res.*, *112*, G02020, doi:10.1029/2006JG000293.
- Vetter, M., et al. (2008), Analyzing the causes and spatial pattern of the European 2003 carbon flux anomaly using seven models, *Biogeosciences*, *5*, 561–583.
- Vitousek, P. M., and R. W. Howarth (1991), Nitrogen limitation on land and in the sea: How can it occur?, *Biogeochemistry*, *13*, 87–115.
- Wang, W., J. Dungan, H. Hashimoto, A. R. Michaelis, C. Milesi, K. Ichii, and R. R. Nemani (2011), Diagnosing and assessing uncertainties of terrestrial ecosystem models in a multimodel ensemble experiment: 2. Carbon balance, *Global Change Biol.*, *17*, 1367–1378, doi:10.1111/j.1365-2486.2010.02315.x.
- Watanabe, S., et al. (2011), MIROC-ESM 2010: Model description and basic results of CMIP5-20c3m experiments, *Geosci. Model Dev.*, *4*, 845–872.
- Wei, Y., et al. (2014), The North American Carbon Program multi-scale synthesis and terrestrial model intercomparison project—Part 2: Environmental driver data, *Geosci. Model Dev. Discuss.*, *6*, 5375–5422.
- Welp, L. R., et al. (2011), Interannual variability in the oxygen isotopes of atmospheric CO₂ driven by El Niño, *Nature*, *477*, 579–582.
- Zaehle, S. (2013), Terrestrial nitrogen-carbon cycle interactions at the global scale, *Philos. Trans. R. Soc., B*, *368*, 20130125, doi:10.1098/rstb.2013.0125.
- Zaehle, S., S. Sitch, B. Smith, and F. Hatterman (2005), Effects of parameter uncertainties on the modeling of terrestrial biosphere dynamics, *Global Biogeochem. Cycles*, *19*, GB3020, doi:10.1029/2004GB002395.
- Zaehle, S., et al. (2007), Projected changes in terrestrial carbon storage in Europe under climate and land-use change, 1990–2100, *Ecosystems*, *10*, 380–401, doi:10.1007/s10021-007-9028-9.
- Zhang, Q., Y. P. Wang, A. J. Pitman, and Y. J. Dai (2011), Limitations of nitrogen and phosphorous on the terrestrial carbon uptake in the 20th century, *Geophys. Res. Lett.*, *38*, L22701, doi:10.1029/2011GL049244.
- Zhang, Y., L. Guanter, J. A. Berry, J. Joiner, C. van der Tol, A. Huete, A. Gitelson, M. Voigt, and P. Köhler (2014), Estimation of vegetation photosynthetic capacity from space-based measurements of chlorophyll fluorescence for terrestrial biosphere models, *Global Change Biol.*, *20*, 3727–3742.
- Zhao, M., and S. W. Running (2010), Drought-induced reduction in global terrestrial net primary production from 2000 through 2009, *Science*, *329*, 940–943.
- Zhao, M., and S. W. Running (2011), Response to comments on “drought-induced reduction in global terrestrial net primary production from 2000 through 2009”, *Science*, *333*, 1093.
- Zhao, M., F. A. Heinsch, R. R. Nemani, and S. W. Running (2005), Improvements of the MODIS terrestrial gross and net primary production global data set, *Remote Sens. Environ.*, *95*, 164–176.
- Zhao, M., S. W. Running, and R. R. Nemani (2006), Sensitivity of Moderate Resolution Imaging Spectroradiometer (MODIS) terrestrial primary production to the accuracy of meteorological reanalyses, *J. Geophys. Res.*, *111*, G01002, doi:10.1029/2004JG000004.
- Zhao, Y., et al. (2012), How errors on meteorological variables impact simulated ecosystem fluxes: A case study for six French sites, *Biogeosciences*, *9*, 2537–2564.
- Zscheischler, J., et al. (2014), Impact of large-scale climate extremes on biospheric carbon fluxes: An intercomparison based on MsTMIP data, *Global Biogeochem. Cycles*, *28*, 585–600, doi:10.1002/2014GB004826.